

The Galactic population of canonical pulsars II

Mattéo Sautron¹, Jérôme Pétri¹, Dipanjan Mitra^{2,3}, and Ludmilla Dirson¹

¹ Université de Strasbourg, CNRS, Observatoire astronomique de Strasbourg, UMR 7550, 67000 Strasbourg, France

² National Centre for Radio Astrophysics, Tata Institute for Fundamental Research, Post Bag 3, Ganeshkhind, Pune 411007, India

³ Janusz Gil Institute of Astronomy, University of Zielona Góra, ul. Szafrana 2, 65-516 Zielona Góra, Poland

Received / Accepted

ABSTRACT

Context. Pulsars are highly magnetized rotating neutron stars, emitting in a broad electromagnetic energy range. These objects have been discovered more than 50 years ago and are astrophysical laboratories for studying physics at extreme conditions. Reproducing the observed population of pulsars refines our understanding of their formation, evolution as well as radiation processes and geometry.

Aims. In this paper, we improve our previous pulsar population synthesis by studying the impact of the Galactic gravitational potential and of the death line putting emphasis on the γ -ray pulsar population. In order to elucidate the necessity of a death line, refined initial distributions for spin periods and radial positions at birth were implemented, elevating the sophistication of our previous simulations to the most recent state-of-the-art.

Methods. The individual motion of pulsars in the Galactic potential is evolved by a fourth order symplectic integration scheme. Our pulsar population synthesis takes into account the secular evolution of a force-free magnetosphere and the magnetic field decay. Each pulsar is evolved from its birth up to the present time. The radio and γ -ray emissions are modeled respectively by the polar cap geometry and the striped wind model.

Results. When simulating a cohort of ten million pulsars akin to previous endeavors, the integration of a death line proves essential for a better agreement with observational trends. Yet, discrepancies emerges when modeling a reduced ensemble of only one million pulsars, endowed with a higher birth rate. This divergence yields a remarkably refined $P - \dot{P}$ diagram, conspicuously with or without any delineating death line. Intriguingly, this observation suggests an overestimation of the ages of detected pulsars in existent data sets, thereby challenging the necessity of death lines in pulsar population synthesis. Validation through Kolmogorov-Smirnov testing underlines the statistical congruence between the spin period and spin period derivative distributions of both observations and simulations. Moreover simulations with a higher γ -ray instrumental sensitivity show that the GeV excess in the Galactic centre could be of pulsar origin.

Key words. pulsars: general - Gravitation - radio continuum: stars - Gamma rays: stars - methods: statistical

1. Introduction

Pulsars, discovered by Jocelyn Bell Burnell in 1967 (Hewish et al. 1968) are rotating neutron stars born in a core-collapsed supernova. Pulsars are highly magnetized and surrounded by a plasma-filled magnetosphere emitting regular pulses of radiation at their spin frequency. Due to the magneto-dipole losses, they lose energy as their spin period increases. Thanks to radio surveys, performed for instance by the Parkes and Arecibo radio-telescopes, nearly 3000 pulsars have been discovered (Manchester et al. 2005) (see Table 1, with the data on the canonical pulsars). Although pulsars were first observed in radio, it was found later that they are also bright in X-rays, optical and gamma-rays. The Large Area Telescope (LAT) on board of the Fermi satellite, has discovered dozens of radio-quiet gamma-ray pulsars as well as millisecond pulsars (MSPs). Since its launch, the LAT has detected about 300 pulsars (Abdo et al. 2013; Smith et al. 2019, 2023). The LAT has unveiled a new perspective, expanding our understanding about pulsars by presenting a growing collection of neutron stars that are detectable through their high energy emission. Moreover, the distinct emission process in high-energy and its unique beaming properties offer an alternative viewpoint on the global pulsar population.

Table 1. Number of known pulsars with spindown luminosity \dot{E} above and below 10^{28} W, and above 10^{31} W. The quantities N_r , N_g , and N_{rg} are the number of radio-only, gamma only, and radio-loud gamma-ray pulsars, respectively. It should be noted that we excluded the binary pulsars as well as pulsars with $P < 20$ ms. The data have been taken from the ATNF catalogue and from <https://confluence.slac.stanford.edu/display/GLAMCOG/Public+List+of+LAT-Detected+Gamma-Ray+Pulsars>

| $\log(\dot{E})$ (W) | N_{tot} | N_r | N_g | N_{rg} |
|---------------------|-----------|-------|-------|----------|
| >31 | 2 | 0 | 0 | 2 |
| >28 | 197 | 101 | 35 | 61 |
| Total | 2665 | 2553 | 63 | 84 |

With the advent of future surveys such as the Square Kilometre Array (SKA ¹) or the Cherenkov Telescope Array (CTA ²), much more pulsars are expected to be detected. Those instruments are scheduled to start collecting data by the end of the decade. SKA is going to be 50 times more sensitive and is predicted to survey the sky 10 000 times faster than any existing imaging radio telescope (McMullin et al. 2020). CTA is aimed at detecting gamma rays in the energy range from a few tens of

¹ <https://www.skao.int/en/science-users/118/ska-telescope-specifications>

² <https://www.cta-observatory.org/about/how-ctao-works/>

GeV up to hundreds of TeV (Hofmann & Zanin 2023) while Fermi/LAT operates in the energy range from 20 MeV to several hundred GeV³.

Pulsar population synthesis (PPS) is a powerful tool aiming at predicting the discovery rate of new pulsars as well as better understanding their emission processes. PPS studies also constrain the overall properties of pulsars. Pulsars are generated from their birth and evolved up to the present. Once the set of pulsars has been generated we check whether they fulfill some prescribed detection criteria. The detectability of an individual pulsar in a given energy band (radio or γ) depends on whether the associated emission beam intersects our line of sight and on the sensitivity of the corresponding instrument.

Most of PPS studies assume that neutron stars are rotating in vacuum (Faucher-Giguère & Kaspi 2006; Popov et al. 2010; Johnston et al. 2020), or take only radio or gamma-ray emission into account (Watters & Romani 2011; Gullon et al. 2014), or assume a constant magnetic field (Gonthier et al. 2002; Faucher-Giguère & Kaspi 2006; Johnston & Karastergiou 2017). For the first time in a PPS study, Dirson et al. (2022) have modeled the population of both the gamma-ray and radio pulsars by taking into account the force-free magnetosphere model in conjunction with the magnetic field decay. The neutron star radiation is produced by relativistic charged particles flowing within their magnetosphere. Therefore it is necessary to take the plasma back reaction into account for the pulsar period and dipole magnetic inclination angle evolution. Whereas the gamma-ray emission site from pulsars is still under debate, different locations have been suggested. These are for instance the polar cap region (Sturrock 1971; Ruderman & Sutherland 1975; Daugherty & Harding 1982, 1996) at low altitudes, the slot gap along the last open magnetic field lines (Arons 1983; Muslimov & Harding 2004; Harding et al. 2008; Harding & Muslimov 2011), or the outer gaps at high altitudes in the outer magnetosphere (Cheng et al. 1986; Hirotani 2008; Takata et al. 2011). The striped wind model, which has for emission site the pulsar wind outside the light cylinder, (Pétri 2009, 2011) is used for the first time by Dirson et al. (2022) in a PPS study. The radio emission is described as usual by the polar cap model.

In this work, and the work of Dirson et al. (2022) only the canonical pulsar population in our Galaxy is reproduced. The canonical pulsar population is defined by isolated pulsars which are not magnetars, and with a spin period greater than 20 ms.

While the study yielded satisfactory results when simulating a population closely resembling the observed pulsar population in the $P - \dot{P}$ diagram, there was room for improvement regarding the pulsar motion. Specifically, the study is limited by the assumption that pulsars move in straight lines at a constant speed from their birth to the present time. A noticeable discrepancy arises when comparing the observed position of pulsars to the simulation expectations, revealing a significant disparity in their spatial distributions.

Since the results obtained by Dirson et al. (2022) did not require the modeling of a death line, it was not included in their PPS. The death line separates in the $P - \dot{P}$ diagram the neutron stars that generate particles through pair cascading from those which cannot radiate anymore and are hence called dead pulsars. This contrasts with the PPS performed by Graber et al. (2023) who did not require a death line. Therefore in this paper we examine the necessity of a death line to explain the observed canonical pulsars population.

This paper improves the PPS of Dirson et al. (2022), questions the necessity of a death line in PPS work and discusses in depth the γ -ray pulsar population. The paper is organised as follows. In Sect. 2 we detail our model, recalling the processes for generation and evolution of the pulsars in the PPS, a description of the Galactic potential, the death line and the multi-wavelength detection criteria. Then the results are shown in Sect. 3. The paper ends with a discussion in Sect. 4 and a summary in Sect. 5.

2. Description of the PPS model

Our PPS study is based on a self-consistent state-of-the-art evolution of the pulsar geometry and proper motion within the Milky Way. In this section we detail the model by exposing first the generation of individual pulsars, their initial position, magnetic field and spin period, then how these quantities should evolve in time, giving explicit expressions for the Galactic potential used in our simulations, before introducing the death line and finally the radio and γ -ray detection criteria.

2.1. Generation of pulsars

We generate a population of pulsars whose ages are generated in ascending order, every X years for example if the birth rate is $1/X \text{ yr}^{-1}$ between 0 yr and the age of the Milky Way at maximum. The age of the Milky Way is almost equal to the age of the Universe, which is of about $t_H \approx 13.8 \times 10^9 \text{ yr}$, therefore, a total number of t_H/X pulsars should be simulated. However as we will see, we chose to emulate 10^7 pulsars in a first run and 10^6 in another run. This choice was made for two reasons : firstly, the computation time is significantly decreased while pulsars older than 10^8 yr are mostly not detected, secondly, the simulation that emulates 10^7 pulsars allows to emulate older pulsars and require a death line while the other works well without. This approach was also chosen because it allows to check whether our birth rate is relevant by comparing our results from the simulation to the observations. It is different from other works like Johnston & Karastergiou (2017) and Gullon et al. (2014), where they stop the simulation when the number of pulsars detected in the simulation are the same as the number of observed pulsars. The value chosen for the birth rate, which is $1/41 \text{ yr}^{-1}$, is taken as best educated guess from the interval $[1/150, 1/33] \text{ yr}^{-1}$ because these studies (Faucher-Giguère & Kaspi 2006; Gullon et al. 2014; Johnston & Karastergiou 2017) evaluated the birth rate of pulsars in this interval.

To describe the position of the pulsars in the Galaxy, we use the right-handed Galacto-centric coordinate system (x, y, z) with the Galactic centre at its origin, y increasing in the disc plane towards the location of the Sun, and z increasing towards the direction of the north Galactic pole. The initial spatial distribution of the pulsars is given by Paczynski (1990). He found two distributions, one describing the radial spread and one the spread in altitude, however only his distribution in altitude is used in our work because the radial distribution in the galactic plane is better depict in Ahlers et al. (2016) by the Milky Way's pulsar surface density defined as

$$\rho(R) = A \left(\frac{R + R_1}{R_\odot + R_1} \right)^a \exp \left(-b \left(\frac{R - R_\odot}{R_\odot + R_1} \right) \right) \quad (1a)$$

$$\rho_z(z) = \frac{e^{-|z|/h_c}}{h_c} \quad (1b)$$

where R is the axial distance from the z -axis, and z is the distance from the Galactic disc. The numerical values for the con-

³ <https://fermi.gsfc.nasa.gov/science/instruments/table1-1.html>

stants are, $A = 37.6 \text{ kpc}^{-2}$, $a = 1.93$, $b = 5.06$, $R_1 = 0.55 \text{ kpc}$, $h_c = 180 \text{ pc}$ and $R_\odot = 8.5 \text{ kpc}$ and in agreement with the distribution of young massive stars in our galaxy (Li et al. 2019). The purpose of choosing equation (1a) to describe the radial spread is to put neutron stars birth positions within the spiral arms of the Galaxy. More precisely the Galactic spiral structure contains four arms with a logarithmic shape function allowing to obtain the azimuthal coordinate ϕ as a function of the distance from the Galactic center

$$\phi(R) = k \ln\left(\frac{R}{r_0}\right) + \phi_0 \quad (2)$$

The values of the models describing each arm are given in Table 2. These values were used by Ronchi et al. (2021) and taken from Yao et al. (2017) to match the shape of the arms of the Galaxy. The local arm is not modeled, because of its very low density, much smaller than the four other arms. Each star has an equal probability to be in one of the four arms, its angular coordinate ϕ for a given R being deduced from (1a). Furthermore, the Galaxy is not static, and its arms are moving with an approximated period $T = 250 \text{ Myr}$ (Skowron et al. 2019). Since we also know that the Galaxy is rotating in the clockwise direction, by knowing the age of a pulsar we can know its angular position at birth. Following the same procedures as Ronchi et al. (2021), in order to avoid artificial features near the Galactic center, noise is added to both coordinates R and ϕ . For instance $\phi_{corr} = \phi_{rand} \exp(-0.35 R)$ where ϕ_{rand} is randomly drawn from a uniform distribution between 0 and 2π . r_{corr} will be taken from a normal distribution with a mean of 0 and a standard deviation $\sigma_{corr} = 0.07 R$ and we add this two corrections to ϕ and R respectively. Therefore $R_{birth} = R + r_{corr}$ and $\phi_{birth} = \phi + \phi_{corr} + \frac{2\pi t_{age}}{T}$, where t_{age} is the age of the pulsar. As soon as R_{birth} and ϕ_{birth} are known we can convert these coordinates in x and y Galactocentric coordinates for each pulsar.

Table 2. Parameters of the Milky Way Spiral Arm structure.

| Arm Number | Name | k (rad) | r_0 (kpc) | ϕ_0 (rad) |
|------------|--------------------|--------------|----------------|-------------------|
| 1 | Norma | 4.95 | 3.35 | 0.77 |
| 2 | Carina-Sagittarius | 5.46 | 3.56 | 3.82 |
| 3 | Perseus | 5.77 | 3.71 | 2.09 |
| 4 | Crux-Scutum | 5.37 | 3.67 | 5.76 |

Next, we need to describe the individual properties of each pulsar, namely, its inclination angle α , which is the angle between its rotation axis and its magnetic axis, its initial spin period and initial magnetic field at birth. The inclination angle α is assumed to follow an isotropic distribution generated from a uniform distribution $U \in [0, 1]$ and given by $\alpha = \arccos(2U - 1)$. In our work, the initial spin period and magnetic field follow both a log-normal distribution, as suggested from the results of a study of 56 young neutron stars by Igoshev et al. (2022) while other works simply use a Gaussian distribution (Faucher-Giguère & Kaspi 2006; Gullon et al. 2014; Johnston et al. 2020). Explicitly, the probabilities to born with an initial magnetic field B_0 and period P_0 are given by

$$p(\log(B_0)) = \frac{1}{\sigma_b \sqrt{2\pi}} e^{-(\log B_0 - \log \bar{B})^2 / (2\sigma_b^2)} \quad (3)$$

$$p(\log(P_0)) = \frac{1}{\sigma_p \sqrt{2\pi}} e^{-(\log P_0 - \log \bar{P})^2 / (2\sigma_p^2)}. \quad (4)$$

The distribution for the magnetic field is identical to the one used in other pulsar population synthesis like for instance Faucher-Giguère & Kaspi (2006), Gullon et al. (2014), Johnston et al. (2020), Yadigaroglu & Romani (1995) and Watters & Romani (2011).

Compared to the study of Dirson et al. (2022) we introduce a novelty, namely the alignment between the kick velocities at birth and the rotation axis of the pulsar, as suggested by Rankin (2007). Moreover according to Hobbs et al. (2005) a Maxwellian distribution best replicates the observations, with a standard deviation $\sigma_v = 265 \text{ km/s}$. The mean velocity of the distribution is related to the standard deviation by $\bar{v} = \sigma_v \sqrt{8/\pi}$. The velocity vector is then distributed along the unit vector of the rotation axis generated as detailed in the subsection 2.5.

2.2. Pulsar evolution

The pulsar initial period, inclination angle and magnetic field must be evolved in time self-consistently due to electromagnetic radiation and internal dissipation within the neutron star. To this end we employ the pulsar force-free magnetosphere model taking into account the plasma current and charge within the magnetosphere. The spin down luminosity \dot{E} is

$$\dot{E} = \frac{dE_{rot}}{dt} = -I\Omega\dot{\Omega} = L_{ff} \quad (5)$$

$$L_{ff} = \frac{4\pi R^6 B^2 \Omega^4 (1 + \sin^2 \alpha)}{\mu_0 c^3} \quad (6)$$

where I is the neutron star moment of inertia its value being approximately $I \approx 10^{38} \text{ kg.m}^2$, $\Omega = 2\pi/P$ is the rotation frequency of the pulsar (P is the spin period) and $\dot{\Omega}$ is its time derivative, $R = 12 \text{ km}$ is the typical radius of a neutron star as found by recent NICER observations (Riley et al. 2019; Bogdanov et al. 2019), B is the magnetic field at the magnetic equator, α is the inclination angle, μ_0 is the vacuum permeability constant, $\mu_0 = 4\pi \times 10^{-7} \text{ H/m}$ and c is the speed of light. The term L_{ff} for the spin down luminosity was given by Spitkovsky (2006) and Pétri (2012). Equation (5) clearly shows the correlation between the obliquity, the magnetic field and the rotation frequency. Combining equation (5) and (6) leads to

$$\dot{\Omega} = -K_{ff} \Omega^n \quad (7)$$

$$K_{ff} = \frac{4\pi R^6 B^2 (1 + \sin^2 \alpha)}{\mu_0 c^3 I} \quad (8)$$

which is written in a more concise form where n is the braking index, its value being $n = 3$ for magnetic dipole radiation.

The integral of motion between Ω and α is also very useful and reads

$$\Omega \frac{\cos^2 \alpha}{\sin \alpha} = \Omega_0 \frac{\cos^2 \alpha_0}{\sin \alpha_0} \quad (9)$$

where quantities with index 0 indicate their initial value. The quantities without the index are their current time value.

As shown by Gullon et al. (2014) a decaying magnetic field better accounts for comparison between pulsar population synthesis and observations. Therefore, we prescribe a magnetic field decay according to a power law

$$B(t) = B_0 (1 + t/\tau_d)^{-1/\alpha_d} \quad (10)$$

where α_d is a constant parameter controlling the speed of the magnetic field decay and $\tau_d = k_{\tau_d} \tau_v$ is the magnetic field decay

time scale. The decay rate τ_v was chosen randomly between 3 values : 5×10^4 yr or 7×10^4 yr or 5×10^5 yr, with a probability of 0.23, 0.46 and 0.31 respectively (these probabilities were chosen as best educated guesses after several run with different values) for each pulsar, corresponding to the τ_v value for canonical pulsars in Viganò et al. (2013). The values of α_d and k_{τ_d} can be found in Table 5 of Sect. 3.

In line with the spin down luminosity, the inclination angle satisfies another evolution equation that after integration was found by Phillipov et al. (2014) for a spherically symmetric neutron star with a constant magnetic field. With our decaying prescription the inclination angle α is found by solving for the root of

$$\begin{aligned} \ln(\sin \alpha_0) + \frac{1}{2 \sin^2 \alpha_0} + K \Omega_0^2 \frac{\cos^4 \alpha_0}{\sin^2 \alpha_0} \frac{\alpha_d \tau_d B_0^2}{\alpha_d - 2} \left[\left(1 + \frac{t}{\tau_d} \right)^{1-2/\alpha_d} - 1 \right] \\ = \ln(\sin \alpha) + \frac{1}{2 \sin^2 \alpha} \end{aligned} \quad (11)$$

where t is the time representing the age of the pulsar and $K = R^6 / I c^3$. The typical decay timescale for a mean magnetic field of 2.5×10^8 T is 4.6×10^5 yr in Viganò (2013), however in this study the typical decay timescale associated to this magnetic field is 3.5×10^5 yr which is consistent with the estimate of Viganò (2013) for the same field strength.

Finally, we need to follow the particle motion within the Galactic potential. Each generated pulsar evolves in the gravitational potential Φ subject to an acceleration $\ddot{\mathbf{x}}$ according to

$$\ddot{\mathbf{x}} = -\nabla\Phi. \quad (12)$$

Equation (12) is integrated numerically thanks to a Position Extended Forest Ruth-Like (PEFRL) algorithm (Peter Young 2014), a fourth order integration scheme, presented in Appendix A with a convergence and accuracy study. The galactic potential model used in discussed in the next section.

2.3. Description of the Galactic potential

The Galaxy is divided in four distinct regions with different mass distributions and associated gravitational potentials. The four potentials are: the bulge Φ_b , the disk Φ_d , the dark matter halo Φ_h and the nucleus Φ_n . The total potential of the Milky Way Φ_{tot} is the sum of these potentials

$$\Phi_{tot} = \Phi_b + \Phi_d + \Phi_h + \Phi_n. \quad (13)$$

The expressions for these potentials are taken from Bajkova & Bobylev (2021) with parameters given in Table 3. The nucleus mass was found in Bovy (2015).

Table 3. Constants values used for the different potentials, with the solar mass $M_\odot = 1.99 \times 10^{30}$ kg.

| Parameters | Values |
|------------|---|
| M_h | $2.9 \times 10^{11} \pm 7.6 \times 10^{10} M_\odot$ |
| a_h | 7.7 ± 2.1 kpc |
| a_d | 4.4 ± 0.73 kpc |
| b_d | 0.308 ± 0.005 kpc |
| M_d | $6.50 \times 10^{10} \pm 1.9 \times 10^9 M_\odot$ |
| a_b | 0.0 kpc |
| b_b | 0.267 ± 0.009 kpc |
| M_b | $1.02 \times 10^{10} \pm 6.3 \times 10^8 M_\odot$ |
| M_n | $4.10^6 \pm 0.42 \times 10^6 M_\odot$ |

The potential for the bulge Φ_b and for the disk Φ_d were both chosen to have the form proposed by Miyamoto & Nagai (1975) which are typically used for models of the gravitational potential of the Milky Way. They read

$$\Phi_i(R, z) = -\frac{GM_i}{\left[R^2 + \left(a_i + \sqrt{z^2 + b_i^2} \right)^2 \right]^{1/2}} \quad (14)$$

where $R^2 = x^2 + y^2$, and $i = b$ is for the bulge and $i = d$ is for the disk. In those formula R depends on the coordinates x and y , a_i and b_i are the scale parameters of the components in kpc, M_i is the mass (for the disk or the bulge) and G is the gravitational constant. The constant values can be found in Table 3.

Solving the pulsar equation of motion requires to compute the gradient of the potentials, the derivatives of the disk and the bulge potentials are

$$\frac{\partial \Phi_i}{\partial x_j} = \frac{GM_i x_j}{\left[R^2 + \left(a_i + \sqrt{z^2 + b_i^2} \right)^2 \right]^{3/2}} \quad (15)$$

$$\frac{\partial \Phi_i}{\partial z} = \frac{GM_i z \left(a_i + \left(z^2 + b_i^2 \right)^{1/2} \right)}{\left[R^2 + \left(a_i + \sqrt{z^2 + b_i^2} \right)^2 \right]^{3/2} \left(z^2 + b_i^2 \right)^{1/2}} \quad (16)$$

x_j being either x or y . Equation (15) is the derivative for the potential of Miyamoto Nagai, where $i = d$ or $i = b$ depending on disk or bulge derivative. Equation (16) is the derivative of the Miyamoto Nagai potential with respect to the z coordinate.

The potential for the dark matter halo Φ_h , according to the frequently used potential of Navarro et al. (1997), it is expressed as

$$\Phi_h(r) = -\frac{GM_h}{r} \ln \left(1 + \frac{r}{a_h} \right) \quad (17)$$

where M_h is the mass of the halo, $r = x^2 + y^2 + z^2$, and a_h is the length scale whose values are found in Table 3. The derivative of equation (17) with respect to any coordinate x_j (x, y, z) is

$$\frac{\partial \Phi_h}{\partial x_j} = \frac{GM_h x_j}{r^2} \left[\frac{1}{r} \ln \left(1 + \frac{r}{a_h} \right) - \frac{1}{r + a_h} \right]. \quad (18)$$

Finally for the last part of the Galaxy, the nucleus of the Milky Way is simply represented by a Keplerian potential Φ_n such as

$$\Phi_n(r) = -\frac{GM_n}{r} \quad (19)$$

where M_n is the mass of the nucleus. The derivative of equation (19) with respect to any coordinate x_j (x, y, z) is given by

$$\frac{\partial \Phi_n}{\partial x_j} = \frac{GM_n x_j}{r^3}. \quad (20)$$

2.4. The death line

Several equations for the death line have been proposed in the literature (Chen & Ruderman 1993; Zhang et al. 2000; Gil & Mitra 2001; Mitra et al. 2019). The most suitable one in our study is that of Mitra et al. (2019) where they found an expression for the death line

$$\dot{P}_{\text{line}} = \frac{3.16 \times 10^{-19} T_6^4 P^2}{\eta^2 b \cos^2 \alpha_l}. \quad (21)$$

Here $T_6 = T/10^6$ K, where T corresponds to the surface temperature of the polar cap. The parameter $\eta = 1 - \rho_i/\rho_{GJ}$ is the electric potential screening factor due to the ion flow, where ρ_i correspond to the ion charge density and ρ_{GJ} to the Goldreich-Julian charge density above the polar cap. The quantity b is the ratio of the actual surface magnetic field to the dipolar surface magnetic field and α_l is the angle between the local magnetic field and the rotation axis. The parameters we used for this death line are : $\alpha_l = 45^\circ$, $b = 40$, $\eta = 0.15$, $T_6 = 2$. Spread in the parameter values of the model causes significant variations in the death line, and thus a death valley rather than a single death line describes the condition for pulsar extinction in the $P-\dot{P}$ diagram.

To decide whether a pulsar is still active in radio, its critical spin down rate \dot{P}_{line} is computed knowing its spin period P . If the pulsar lies in the death valley defined by the inequality $10^{-0.55} < \dot{P}_{\text{line}}/\dot{P} < 10^{1.15}$ then a value for α_l is taken from a uniform distribution between 0° and 65° . Moreover a value for T_6 is also taken from a uniform distribution between 1.9 and 2.8. The parameter b is taken from a uniform distribution between 30 and 60. The boundary parameter values for the death valley were chosen to traverse the $P-\dot{P}$ diagram from the region in the bottom right quadrant where the density starts to decrease, to the detectable pulsar with the lowest \dot{P} and highest P in the same quadrant, as shown in Fig. 1. The edges of the death valley given by the values $10^{-0.55}$ and $10^{1.15}$ were found by taking the extreme values for the parameters that are drawn from the different uniform distributions. Then we compare its actual spin down rate \dot{P} , computed from the evolution model, to the $\dot{P}_{\text{line}}^{\text{new}}$ computed with equation (21) with the parameters which were drawn from uniform distributions. For pulsars that are not in the death valley, their \dot{P} is only compared with the spin down rate \dot{P}_{line} obtained with the default parameters. If the pulsar has its \dot{P} , which was computed from the evolution model, below the one computed with the death line (\dot{P}_{line} or $\dot{P}_{\text{line}}^{\text{new}}$), then the pulsar is considered as dead, otherwise it is considered as still emitting photons. These choices were made in order to have more like a death valley near the death line than a strict condition of death, because the parameters T_6 , α_l and b may be different from one pulsar to another.

2.5. Detection

For each generated pulsar, we check whether it fulfills the criteria for detection depending on three factors. First, the beaming fraction indicates the fraction of the sky covered by the radiation beam and depends on the considered wavelength, here radio or γ -ray. The beaming fraction varies also with the pulsar spin rate, geometry and location of the emission regions. Before explaining how the beaming fraction in radio and in γ -ray are computed, it is important to define several angles.

The angle between the line of sight and the rotation axis is denoted by $\xi = (\hat{n}_\Omega, \hat{n})$ where $\hat{n}_\Omega = \Omega/\|\Omega\|$ is a unit vector along the rotation axis and \hat{n} the unit vector along the line of sight. The inclination angle $\alpha = (\hat{n}_\Omega, \hat{\mu})$ is the angle between the

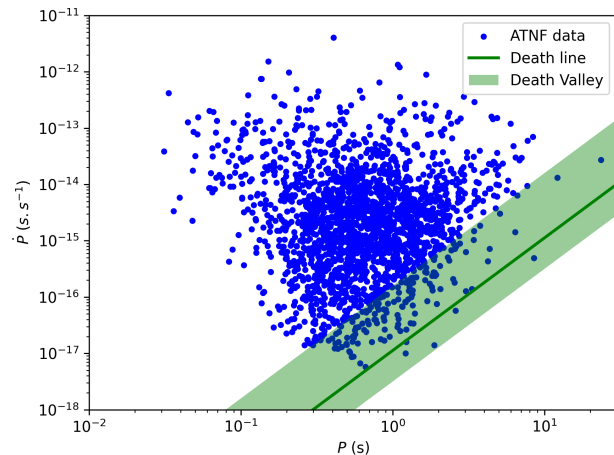


Fig. 1. $P-\dot{P}$ diagram of the canonical pulsars along with the death line, green solid line, and death valley, shaded green area.

rotation axis and the magnetic moment, $\hat{\mu}$ being the unit vector along the magnetic moment. Traditionally the impact angle is also introduced as the angle between the magnetic moment and the line of sight $\beta = (\hat{\mu}, \hat{n})$. Moreover, it is related to the previous angles by $\alpha + \beta = \xi$.

We choose a isotropic distribution for the Earth viewing angle ξ as well as for the orientation of the unitary rotation vector. The Cartesian coordinates of the unit rotation vector \hat{n}_Ω are $(\sin \theta_{n_\Omega} \cos \phi_{n_\Omega}, \sin \theta_{n_\Omega} \sin \phi_{n_\Omega}, \cos \theta_{n_\Omega})$. We set the Sun position at $(x_\odot, y_\odot, z_\odot) = (0 \text{ kpc}, 8.5 \text{ kpc}, 15 \text{ pc})$ (Siegert 2019). The coordinates for \hat{n} are

$$\hat{n} = \left(\frac{x - x_\odot}{d}, \frac{y - y_\odot}{d}, \frac{z - z_\odot}{d} \right). \quad (22)$$

To compute the pulsar distance from Earth, we use the formula for the distance which is

$$d = \sqrt{(x - x_\odot)^2 + (y - y_\odot)^2 + (z - z_\odot)^2}. \quad (23)$$

2.5.1. Radio detection model

The beaming fraction in radio depends on the half opening angle of the radio emission cone ρ computed according to

$$\rho = 3 \sqrt{\frac{\pi h_{\text{em}}}{2Pc}} \quad (24)$$

where h_{em} is the emission height, P is the spin period of the pulsar and c is the speed of light. The emission height is taken constant with an average value of $h_{\text{em}} = 3.10^5$ m, estimated from observations of a sample of pulsars by (Weltevrede & Johnston 2008; Mitra 2017; Johnston & Karastergiou 2019; Johnston et al. 2023). The cone half-opening angle ρ estimated in eq. (24) holds only for the last open field lines of a magnetic dipole and can only be applied for slow pulsars where the radio emission altitude is high enough for the multipolar components to decrease significantly and become negligible.

The pulsar is detected in radio if $\beta = |\xi - \alpha| \leq \rho$ or if $\beta = |\xi - (\pi - \alpha)| \leq \rho$ corresponding to the north and south hemisphere respectively. It must also satisfy the condition $\alpha \geq \rho$ and $\alpha \leq \pi - \rho$ in order to effectively see radio pulsation, because the line of sight must cross the emission cone to observe pulsations.

Another useful quantity is the observed width of the radio profile w_r which is computed as (see Lorimer & Kramer (2004))

$$\cos(\rho) = \cos(\alpha) \cos(\xi) + \sin(\alpha) \sin(\xi) \cos(w_r/2). \quad (25)$$

The second factor for detection is the luminosity, which is also different between radio and gamma-rays. First, concerning the radio flux density, the formula used is the same as in Johnston et al. (2020) for a pulsar at 1.4 GHz, in order to model the detection carried out by the Parkes radio telescope in the Southern Galactic plane (Kramer et al. 2003; Lorimer et al. 2006; Cameron et al. 2020) and the Arecibo telescope in the northern plane (Cordes et al. 2006)

$$F_r = 9 \text{ mJy} \left(\frac{d}{1 \text{ kpc}} \right)^{-2} \left(\frac{\dot{E}}{10^{29} \text{ W}} \right)^{1/4} \times 10^{F_j} \quad (26)$$

where d is the distance in kpc and F_j is the scatter term which is modeled as a Gaussian with a mean of 0.0 and a variance of $\sigma = 0.2$. The detection threshold in radio is set by the signal to noise ratio defined by

$$S/N = \frac{F_r}{S_{\text{survey}}^{\text{min}}}. \quad (27)$$

The pulsar is detected if the signal to noise ratio S/N is greater or equal to 10. $S_{\text{survey}}^{\text{min}}$ is the minimum flux which is related to the period of rotation P , the width profile of radio emission w_r and the sensitivity of the survey which is the last factor for detection, and will be detailed later. We directly compute the radio flux, without computing the luminosity in radio which overlooks the fact that the luminosity received will depend on the geometry of the beam.

The third and last factor is the sensitivity, depending on the survey, therefore on the instrument used and on the pulse profile observed. A pulsar is detected in radio if the signal to noise ratio is greater than 10, but this ratio depends on the minimum flux, another function of the instrumental sensitivity. With the aim of computing the observed width pulse profile, we use the same formula as Cordes & McLaughlin (2003)

$$\tilde{w}_r = \sqrt{\left(w_r \frac{P}{2\pi} \right)^2 + \tau_{\text{samp}}^2 + \tau_{DM}^2 + \tau_{\text{scat}}^2} \quad (28a)$$

$$S_{\text{survey}}^{\text{min}} = S_0 \sqrt{\frac{\tilde{w}_r}{P - \tilde{w}_r}} \quad (28b)$$

Equation (28a) takes into account density fluctuations in the interstellar medium (ISM), the dispersion and scattering during the propagation of the radio pulse when interacting with the free electrons. Moreover, the instrumental effect is also taken into account with τ_{samp} , which is the sampling time of the instrument. All this mechanisms lead to a broader pulse profile. In order to determine the influence of the ISM through τ_{DM} , the formula of Bates et al. (2014) is used

$$\tau_{DM} = \frac{e^2 \Delta f_{ch} DM}{\pi m_e c f^3} \quad (29)$$

e is the electron charge, m_e its mass, Δf_{ch} the width of frequency of the instrument channel, f the observing frequency and DM the dispersion measure. Furthermore, in order to determine the influence of scattering by an inhomogeneous and turbulent ISM through τ_{scat} , the empirical fit relationship from Krishnakumar et al. (2015) is used

$$\tau_{\text{scat}} = 3.6 \times 10^{-9} DM^{2.2} (1 + 1.94 \times 10^{-3} DM^2). \quad (30)$$

Both τ_{DM} and τ_{scat} depend on the dispersion measure, which is found for each pulsar by running the code of Yao et al. (2017) converting the distance of a pulsar into the dispersion measure thanks to their state-of-the art model of the Galactic electron density distribution. The radio survey parameters used are the ones from the Parkes Multibeam Pulsar Survey (PMPS), see Table 4.

Table 4. Survey parameters of the Parks Multibeam Pulsar Survey (PMPS).

| Δf_{ch} (kHz) | f (GHz) | τ_{samp} (μs) |
|--------------------------|--------------|---|
| 3000 | 1.374 | 250 |

Concerning equation (28b), S_0 represents the survey parameters. Johnston et al. (2020) estimated that S_0 should approximately be equal to 0.05 mJy to have a signal to noise ratio greater than 10 for normal pulsars in this survey. We chose equation (28b) to compute the minimum flux, to decide whether a pulsar will be detected in radio or not, however it does not reproduce the whole complexity of this quantity which could be computed more precisely, (see equation (24) of Faucher-Giguère & Kaspi (2006) for instance, where S_0 is computed more precisely) even though it remains a good approximation. In addition we only use the parameters of PMPS to compute τ_{DM} , we could have also used the parameters of The Pulsar Arecibo L-band Feed Array (PALFA) Survey, however the differences in the results in the end are not large if we use these parameters, consequently, it persists as a favorable approximation to exclusively utilize the parameters delineated by PMPS.

2.5.2. Gamma-ray detection model

The γ -ray emission model relies on the striped wind model, describing gamma-ray photons production emanating from the current sheet within the striped wind. In order to detect the gamma-ray, the line of sight of the observer must remain around the equator plane with an inclination angle constrained by $|\xi - \pi/2| \leq \alpha$. The gamma-ray luminosity is extracted from a study of Kalapotharakos et al. (2019), where they showed that the luminosity is described by a fundamental plane. The 3D model depends on the magnetic field B , the spin down luminosity \dot{E} and the cut-off energy ϵ_{cut} . However, in our PPS the cut-off energy is not computed therefore we use their two dimensional version

$$L_{\gamma(2D)} = 10^{26.15 \pm 2.6} W \left(\frac{B}{10^8 \text{ T}} \right)^{0.11 \pm 0.05} \left(\frac{\dot{E}}{10^{26} \text{ W}} \right)^{0.51 \pm 0.09} \quad (31)$$

The spindown \dot{E} is computed with equation (5) and the associated γ -ray flux detected on earth is computed with

$$F_\gamma = \frac{L_{\gamma(2D)}}{4\pi f_\Omega d^2} \quad (32)$$

where f_Ω is a factor depending on the emission model reflecting the anisotropy. For the striped wind model Pétri (2011) showed that this factor varies between 0.22 and 1.90. Nevertheless, an approximation is made : if $\alpha < -\xi + 0.6109$ then $f_\Omega = 1.9$ otherwise $f_\Omega = 1$. The pulsar is detected in gamma depending on the instrumental sensitivity as described below.

The sensitivity in gamma-ray is based on the expectation of the Fermi/LAT instrument ⁴. Two conditions are required

⁴ https://fermi.gsfc.nasa.gov/ssc/data/analysis/documentation/Cicerone/Cicerone_LAT_IRFs/LAT_sensitivity.html

to count the detection, first we need a sufficient value for the flux. If the galactic latitudes of the pulsar is $< 2^\circ$, then $F_{\min} = 4 \times 10^{-15} \text{ W.m}^{-2}$, and if blind searches are assumed we set $F_{\min} = 16 \times 10^{-15} \text{ W.m}^{-2}$. Hence, if the gamma-ray flux F_γ is greater than F_{\min} , the pulsar is detected in gamma-rays if the second condition is fulfilled. Moreover, in order to take the ISM into account, we set a threshold on the dispersion measure DM (a similar approach was done in Gonthier et al. (2018) for millisecond gamma-ray pulsars) because gamma-ray canonical pulsars typically originate from supernova explosions and are associated with regions of recent star formation, such as supernova remnants or star-forming regions. These environments can have higher densities of free electrons in the interstellar medium (ISM), leading to higher DM values for pulsars in these regions. Since gamma-rays pulsars are often young, they are likely still remaining in these regions. Adjusting the DM threshold can help optimize the balance between maximizing sensitivity to pulsar signals and minimizing contamination from background sources. Therefore, the DM threshold chosen is $15 \text{ cm}^{-3}.\text{pc}$, following the lowest DM in the ATNF catalogue for high-energy pulsars.

3. Results

Let us now move to the PPS simulation results. First we show runs simulating 10 million pulsars with and without a death line, allowing to simulate old pulsars (with the oldest aged $4.1 \times 10^8 \text{ yr}$). Then we show runs simulating 1 million pulsars (with the oldest aged $4.1 \times 10^7 \text{ yr}$) with and without considering a death line. We explore a possible spin-velocity misalignment effect due to the galactic potential and the impact of the initial spin period distribution, normal vs log-normal. Finally, the gamma-ray simulations and detection are discussed in details.

3.1. Simulating 10 millions pulsars

3.1.1. Without a death line

The first simulations performed with the Galactic potential implemented discarded the death line. The parameters used for these runs are given in Table 5. The total number of pulsars is summarized in Table 6. The quantities N_r , N_g , and N_{rg} are the

Table 5. Parameters used in the simulations.

| τ_{birth} (1/yr) | P_{mean} (ms) | B_{mean} (T) | σ_p | σ_b | α_d | k_{τ_d} |
|------------------------------|------------------------|-----------------------|------------|------------|------------|--------------|
| 41 | 129 | 2.75×10^8 | 0.45 | 0.5 | 1.5 | 5 |

Table 6. Number of pulsars detected without the implementation of the death line.

| $\log(\dot{E})$ (W) | N_{tot} | N_r | N_g | N_{rg} |
|---------------------|------------------|-------|-------|----------|
| >31 | 11 | 0 | 8 | 3 |
| >28 | 161 | 9 | 75 | 77 |
| Total | 2653 | 2336 | 139 | 178 |

number of radio-only, gamma-only, and radio-loud gamma-ray pulsars, respectively, obtained from our simulation.

Compared to the results obtained by Dirson et al. (2022), at very high spin down luminosity, $\dot{E} > 10^{31} \text{ W}$, the detection is almost identical but at $\dot{E} > 10^{28} \text{ W}$ there are much less pulsars detected in radio and radio/gamma in this work. There are probably two causes for this discrepancy in the number of detected

pulsars at $\dot{E} > 10^{28} \text{ W}$: firstly the difference in the spin period distribution at birth. Pulsars have a higher probability to start with a higher P_0 since the mean of the distribution is higher (in the previous study the mean was 60 ms while it is 129 ms now), therefore the slowing down of the pulsars can only decrease their rotation frequency Ω , and equation (5) shows that \dot{E} depends on Ω . However, it does not affect the detection in gamma-rays because usually canonical gamma pulsars have a high \dot{P} and a low P , being young, therefore their \dot{E} is higher than for radio pulsars. Secondly, the ISM dispersion and scattering reduces this number of radio pulsars detected (the results without the ISM effect are not shown but without it there is much more radio pulsars detected). Nonetheless, in terms of total number of detected radio pulsars, the Galactic potential allows to have an increase compared to the number found in Dirson et al. (2022), a result expected because of the attractive nature of the potential of the Galaxy. In its previous version the PPS moved the pulsars in random spatial directions at constant speed, as a result no pulsar was bound to the Milky Way in closed orbits this is especially true for old pulsars which could have time to leave the Galaxy.

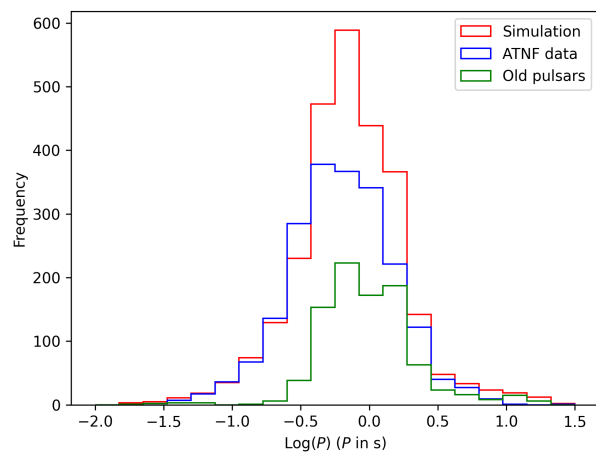


Fig. 2. Distribution of the observed period taken from the ATNF catalogue, along with the simulations without the implementation of the death line. In green, the period of the simulated pulsars with age greater than $10^{7.5}$.

Fig. 2 shows the distribution of the spin period of the detected pulsars in the simulation, in red and in observations, in blue. However the comparison is not satisfactory because there is an excess of pulsars detected in the simulation. Furthermore, this excess is also present in Fig. 3 where the age of the detected pulsars from the observations and simulation are plotted.

In order to verify if there is a correlation between old pulsars and the ones with a high spin period, we plotted in Fig. 2, in green the pulsars with an age greater than $10^{7.5} \text{ yr}$, corresponding to the oldest pulsars of the simulation and it corresponds to the excess found in Fig. 2. Due to the Galactic potential, more pulsars remain bound to the Galaxy, especially older pulsars which were escaping the Galaxy more easily in the work of Dirson et al. (2022) because of the absence of potential. Fig. 4 shows that many pulsars are in what is commonly called the graveyard of pulsars at the bottom right of the $P - \dot{P}$ diagram.

Given this excess of long period pulsars without a death line, we decided to implement one, in order to stick closer to reality.

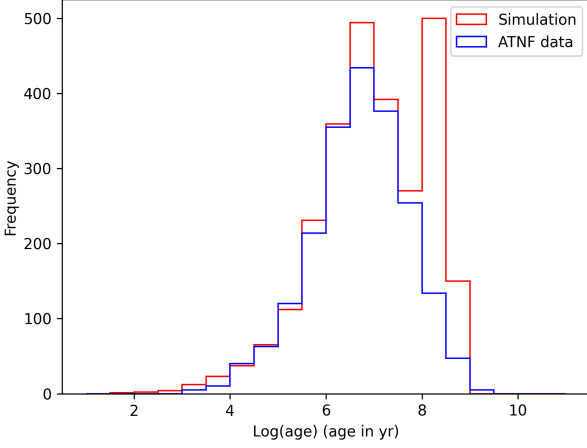


Fig. 3. Distribution of the observed age taken from the ATNF catalogue, along with the simulations without the implementation of the death line.

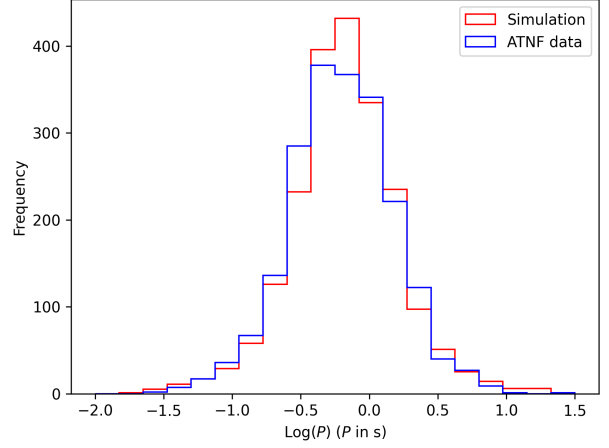


Fig. 5. Distribution of the observed period taken from the ATNF catalogue, along with the simulations with the death line implementation.

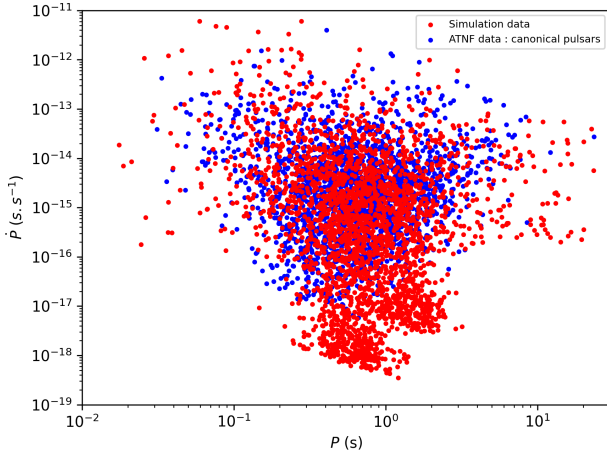


Fig. 4. $P - \dot{P}$ diagram of the simulated population, along with the observations, without the implementation of the death line.

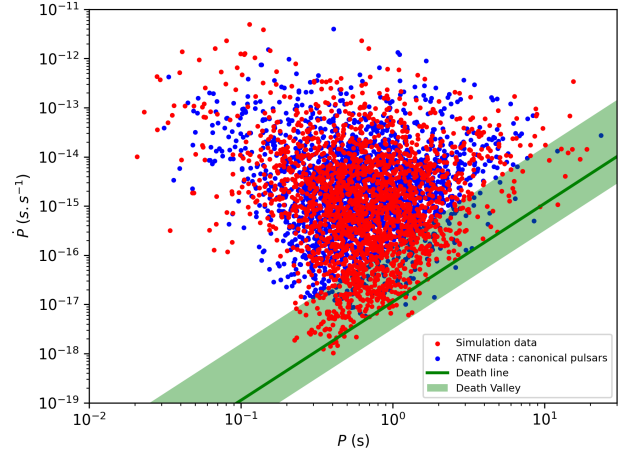


Fig. 6. $P - \dot{P}$ diagram of the simulated population, along with the observations, with the death line implementation.

3.1.2. With the death line

Adding a death line decreases the number of pulsars detected in radio compared to the situation without a death line, see Table 7.

Table 7. Number of pulsars detected with the death line implementation.

| $\log(\dot{E})$ (W) | N_{tot} | N_r | N_g | N_{rg} |
|---------------------|-----------|-------|-------|----------|
| >31 | 10 | 0 | 5 | 5 |
| >28 | 118 | 7 | 69 | 42 |
| Total | 2077 | 1807 | 116 | 154 |

The death line improves the fit as seen in Fig. 5 for the distribution of spin period and compared with Fig. 2, even though there is a slight excess of pulsars which have spin period between $10^{-0.5}$ s and 1 s. In Fig 6, these pulsars in excess lie at \dot{P} between 10^{-18} and 10^{-17} , where there is no data and which correspond to the oldest pulsars in the simulation. Therefore the oldest pulsars simulated here do not correspond to any real data.

In addition, there are too many pulsars close to the death line compared to the observations, there is a pile up effect created by the death line which is not in the observations.

The goodness-of-fit can be checked using a density plot of the $P - \dot{P}$ diagram as in Johnston & Karastergiou (2017) instead of putting points for individual pulsars. In order to construct such diagrams we binned the data evenly in a log scale in P and \dot{P} and count the number of pulsars in each bin. This leads to a 2D histogram to be compared with the observed density plot 2D histogram. Because the total number of simulated pulsars $N_{tot\sim}$ is different from the total number of observed pulsars $N_{tot\obs}$, we normalise the number of pulsars in each bin in order to compare proportions. We therefore introduce the quantity R as follows

$$R = \frac{N_{sim}/N_{tot\sim} - N_{obs}/N_{tot\obs}}{N_{sim}/N_{tot\sim} + N_{obs}/N_{tot\obs}}. \quad (33)$$

With this definition the number R remains in the interval $[-1, +1]$. N_{sim} is the number of pulsar count in a bin of the simulation, N_{obs} the number of pulsar detected in a bin of the observations. A good fit in a bin correspond to a value of R close to 0, meaning that the simulation results are close to the observations.

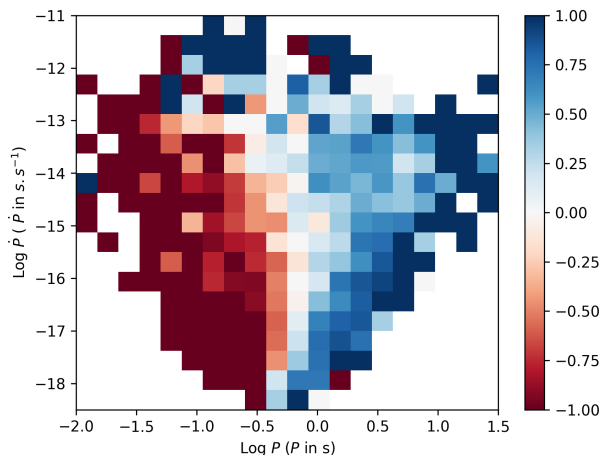


Fig. 7. Density plot of the $P - \dot{P}$ diagram in comparison with observations

Inspecting fig. 7, we note a stronger deviation from the observations at the boundaries of the density plot, for instance it confirms too many pulsars are piling up close to the death line. The high values of R at these boundaries originates from the weak number of pulsars counted in this bins leading to bad statistics and large variations in the proportions, a side effect of the density plot approach. The fact that the colors are very dark, shows that the proportion of pulsars in most of the bins are not good.

A Kolmogorov Smirnov (KS) test (Smirnov 1948) was conducted on both P and \dot{P} which gave p-values substantially below 0.05 respectively when no death line is implemented. While we obtained p-values of 0.05 and another one well below 0.05 respectively for P and \dot{P} with a death line implementation. The null hypothesis that observations and simulations originate from the same distribution for the spin period can not be rejected (p-value ≥ 0.05) only when a death line is considered, but is clearly rejected for \dot{P} in both case.

3.2. Simulating 1 millions pulsars

3.2.1. With the death line

The parameters used for these runs are shown in Table 5. This new set of simulations is intended to verify if generating pulsars younger than 4.1×10^7 yr is sufficient, since we observe a small excess of very old pulsars. The death line is also taken into account.

Table 8. Number of pulsars detected with the death line implementation for 1 million pulsars simulated.

| $\log(\dot{E})$ (W) | N_{tot} | N_r | N_g | N_{rg} |
|---------------------|-----------|-------|-------|----------|
| >31 | 2 | 0 | 2 | 0 |
| >28 | 124 | 7 | 73 | 44 |
| Total | 1694 | 1414 | 154 | 126 |

Table 8 shows that a few less pulsars were detected in this simulation compared to the one with the death line and 10 millions pulsars (see Table 7). Moreover, inspecting the histograms for spin period and spin period derivative respectively in Fig. 8 and 9, we conclude that observations and simulations are very similar in both histograms. A KS test was conducted for both distributions P and \dot{P} and yielded p-values of 0.24 and 0.07 re-

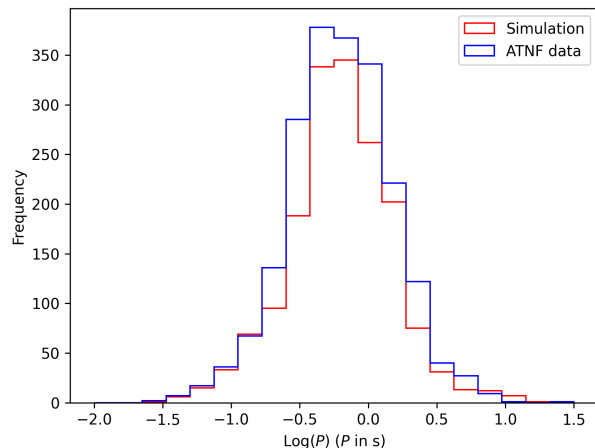


Fig. 8. Distribution of the observed period taken from the ATNF catalogue, along with the simulations with the death line implementation for 1 million pulsars simulated.

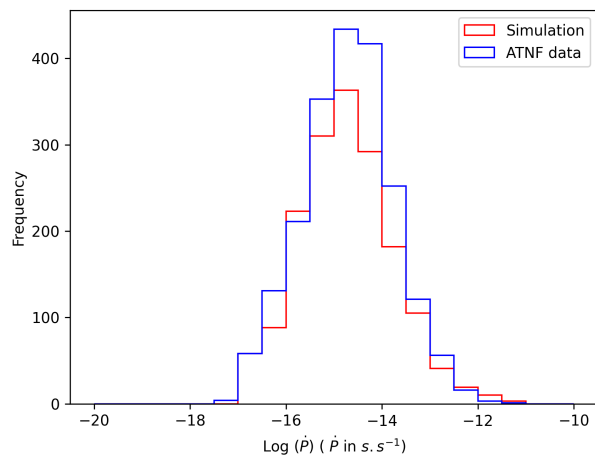


Fig. 9. Distribution of the observed period derivative taken from the ATNF catalogue, along with the simulations with the death line implementation for 1 million pulsars simulated.

spectively. Therefore, it is impossible to reject the null hypothesis that the simulated distributions are similar to the observed distribution.

Fig 10 shows the good agreement between simulations and observations. Furthermore, we can compare now Fig. 11 and Fig. 7. It is obvious that Fig. 11 is better, because globally the colors are lighter which signifies the proportion of pulsars in each 2D bin are almost alike. In addition, there is not a pile up effect anymore next to the death line, which corresponds better to the data.

The distribution of the distance to Earth is shown in Fig. 12. It has a slightly better similarity to the observations than the work of Dirson et al. (2022). Nevertheless the improvement is marginal compared to the improvements of P and \dot{P} histograms. However, we noticed that removing the effect of dispersion and scattering of the ISM on the radio pulse profile, we would obtain very similar distribution of distances between observations and simulations. Therefore, a refinement in the description of the effect of the ISM on the pulse profile might be necessary.

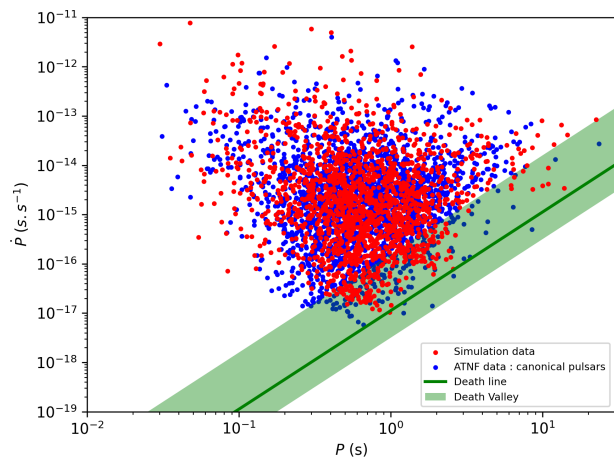


Fig. 10. $P - \dot{P}$ diagram of the simulated population, along with the observations, with the death line implementation for 1 million pulsars simulated.

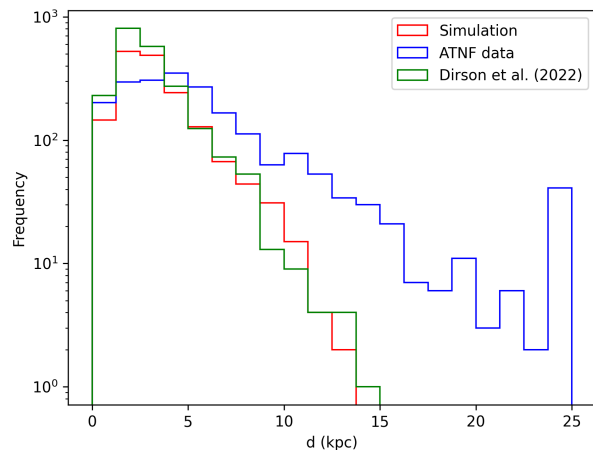


Fig. 12. Distance distribution to Earth for observed and simulated populations (1 million pulsars), including the death line implementation.

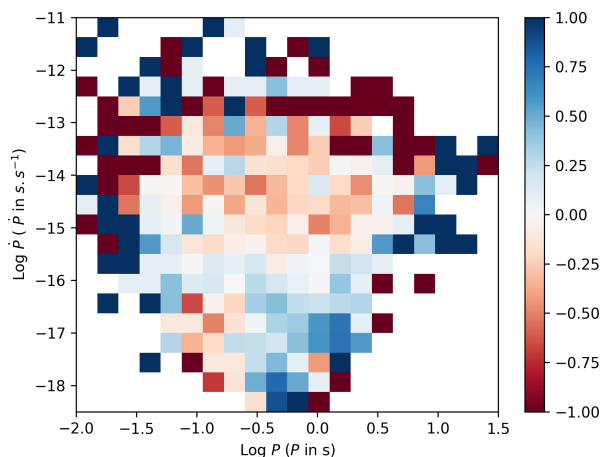


Fig. 11. Density plot of the $P - \dot{P}$ diagram in comparison with observations for 1 million pulsars simulated.

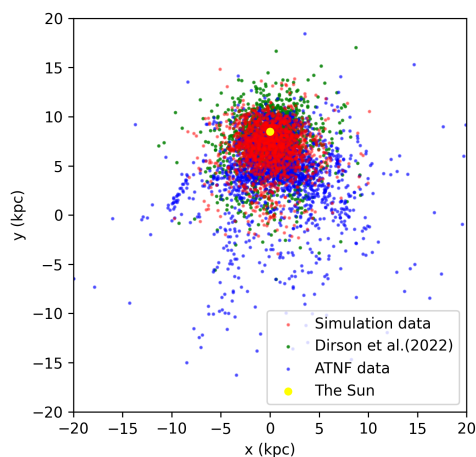


Fig. 13. Spatial distribution of the simulated pulsars, along with the observations, projected onto the Galactic plane for 1 million pulsars simulated.

Indeed, Fig. 13 confirms that the positions of the pulsars in the X-Y plane of the Galaxy are slightly more scattered than before, but the improvement is marginal.

Finally fig. 14 compares the Galactic latitudes from the previous study (see Fig. 9 of Dirson et al. (2022)), now the simulated distribution resembles more the observations, especially around all the latitudes that are different from 0° . Therefore, the Galactic potential helped tracking the pulsar trajectories more realistically.

3.2.2. Without a death line

Because the simulation where 1 million pulsars are simulated do not allow to obtain pulsars older than 4.1×10^7 yr, we undertook a thorough examination of the usefulness of a death line in modeling the canonical pulsar population. Upon conducting simulations with and without a death line (see Table 5 for the parameter values used in the simulations), it emerged that the resultant number of detected pulsars and the corresponding plots exhibited remarkable similarities. In addition, when we conduct

the KS test on P and \dot{P} between 2 simulations with and without death line, we get p-values of 0.71 and 0.16 respectively, which confirms the similarity between the two simulations. Consequently, our attention turned towards exploring the impact of lower birth rates to ascertain if they provide a more congruous fit for both spin period and spin period derivative distributions.

Running simulations with a birth rate of $1/70 \text{ yr}^{-1}$ or a birth rate of $1/150 \text{ yr}^{-1}$ (as a consequence, increasing the oldest simulated pulsar), conspicuously revealed an insufficient number of detected pulsars in both Fig. 15 and Fig. 16. Intriguingly, a discernible paucity of pulsars congregating in the bottom right quadrant of the diagram, colloquially known as the pulsar graveyard, persisted even under these conditions, therefore regardless of the birth rates, thus casting doubt on the necessity of a death line in this configuration. Ultimately, our analysis underscores the pivotal importance of delineating the maximum age of simulated pulsars, as elucidated in Subsection 3.1, while the incorporation of a death line do not seem indispensable for attaining realistic results when simulating 1 million pulsars.

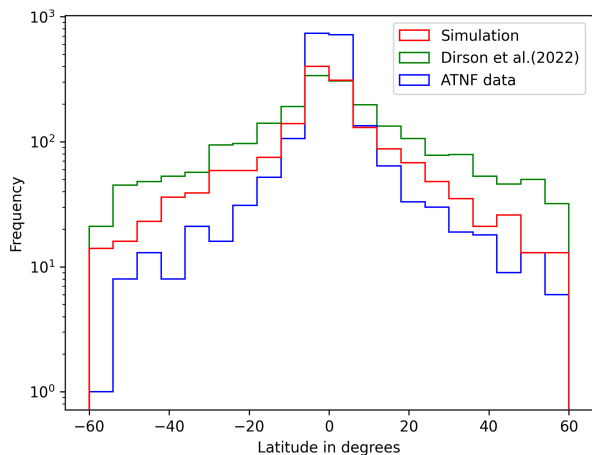


Fig. 14. Distribution of the observed latitude taken from the ATNF catalogue, along with the simulations with the death line implementation for 1 million pulsars simulated.

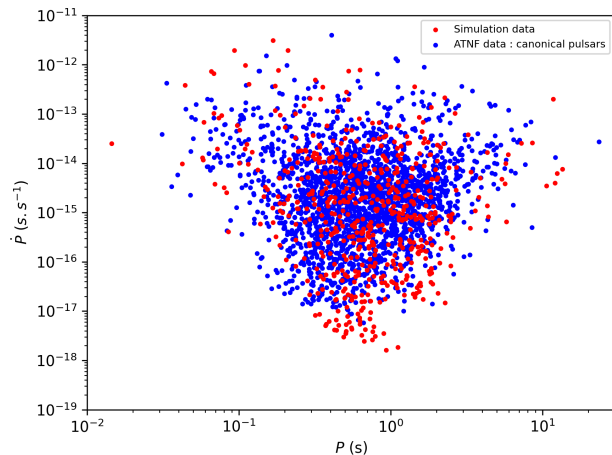


Fig. 16. $P - \dot{P}$ diagram of the simulated population, along with the observations, without death line implementation, birth rate of $1/150 \text{ yr}^{-1}$ for 1 million pulsars simulated.

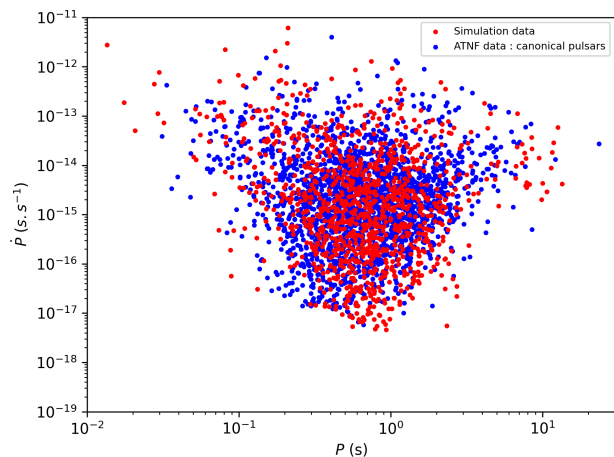


Fig. 15. $P - \dot{P}$ diagram of the simulated population, along with the observations, without death line implementation, birth rate of $1/70 \text{ yr}^{-1}$ for 1 million pulsars simulated.

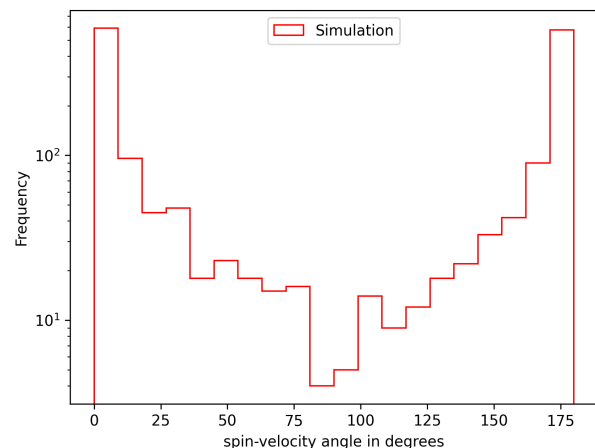


Fig. 17. Distribution of the spin-velocity angles for all the detected pulsars in the simulation for 1 million pulsars simulated.

3.3. Spin-velocity misalignment effect

With the aim of observing the effect of the Galactic potential, we looked at the alignment of the rotation axis and the proper motion velocities of the pulsars. Results are taken from the simulation containing 1 million pulsars, see Table 5 for the parameters used. Noutsos et al. (2013) showed by studying a catalog of 58 pulsars that pulsars younger than 10 Myr keep their rotation axis and their velocities vector still aligned or anti-aligned, because they were aligned at birth according to Rankin (2007). Meanwhile, pulsars older than 10 Myr do not show this trend anymore. This progressive misalignment effect is due to the movement through the Galactic potential.

Fig. 17 demonstrates that most pulsars have their rotation axis aligned with their velocities, but for spin-velocity angles between 25° and 180° the numbers of pulsars is considerably lower than around 0° and 180° . On the one hand, for pulsars younger than 10 Myr, shown in blue in Fig. 18, only a small fraction of pulsars have their spin-velocity angle greater than 25° and below 150° . On the other hand, for pulsars older than 10 Myr, shown

in red in Fig. 18, their spin-velocity angle becomes greater than 25° or below 150° .

Furthermore, in Fig. 19, we can confirm that, the older the pulsar is, the better is its chance to orbit more in the Galaxy, allowing it to deviate its spin-velocity angle from alignment (or anti-alignment). In addition, even if the pulsar is not that old, if it made many orbits in the Galaxy, its spin-velocity angle will be between 25° and 150° , which confirms the fact that its the Galactic potential (and not only age) which makes this spin-velocity angle increase (or decrease if its is anti-aligned at birth). In the contrary, there are pulsars which are old which did not made many orbits in the Galaxy, as a consequence they have their spin-velocity angle near 0° or 180° . These plots clearly shows the influence of the Galactic potential making the pulsars lose their alignment between their rotation axis and their velocities through time because they evolve in the Galactic potential.

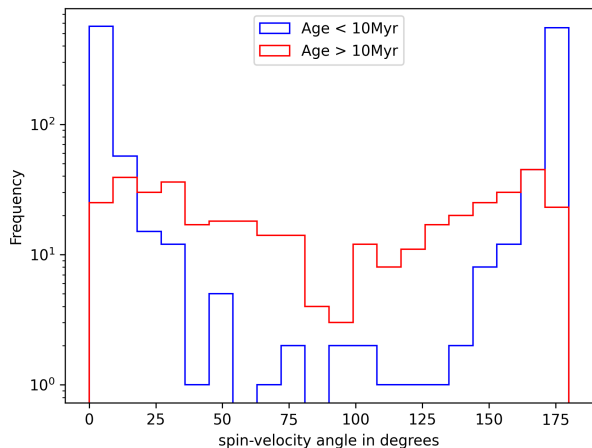


Fig. 18. Distribution of the spin-velocity angles for the detected pulsars younger than 10 Myr (blue) and pulsars older than 10 Myr (red) in the simulation.

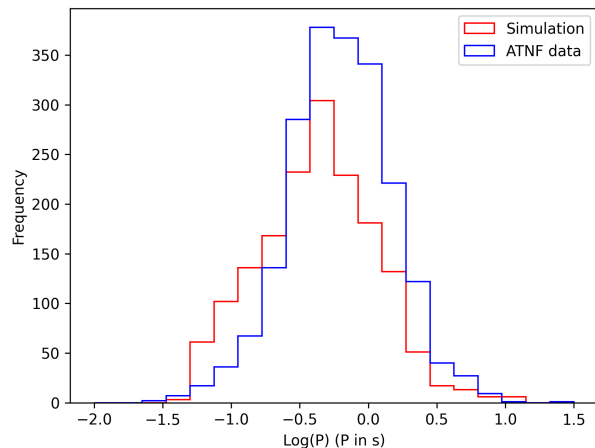


Fig. 20. Distribution of the observed period taken from the ATNF catalogue, along with the simulations with the death line implementation and the Gaussian distribution at birth for the spin period.

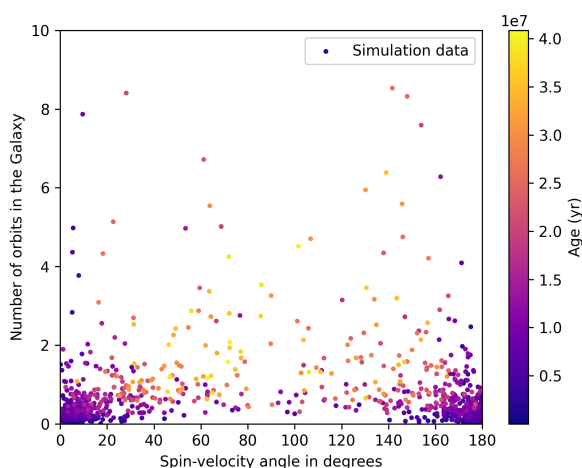


Fig. 19. The spin-velocity angles for the detected pulsars in function of the number of orbits made by the pulsars.

3.4. Log normal vs normal distribution for spin period at birth

Table 9. Number of pulsars detected with the death line implementation and the Gaussian distribution at birth for the spin period.

| $\log(\dot{E})$ (W) | N_{tot} | N_r | N_g | N_{rg} |
|---------------------|-----------|-------|-------|----------|
| >31 | 7 | 0 | 5 | 2 |
| >28 | 275 | 9 | 138 | 128 |
| Total | 1642 | 1188 | 223 | 231 |

In order to estimate the impact of a new distribution of spin period at birth, we compare the results with the previous distribution of spin period

$$p(P_0) = \frac{1}{\sigma_p \sqrt{2\pi}} e^{-(P_0 - \bar{P})^2 / (2\sigma_p)^2} \quad (34)$$

The simulation in this subsection uses $\bar{P} = 60$ ms and $\sigma_p = 10$ ms as parameters of equation (34). The Galactic potential and

the death line were both taken into account to compare the influence of the initial spin period distribution and 1 million pulsars were simulated, see Table 5 for the parameters used.

Table 9 highlights the fact that much more pulsars are detected above $\dot{E} > 10^{28}$ W compared to the simulation with the Gaussian in log space for the spin period, see Table 7. It confirms the suspicion that the distribution of initial spin period influences the number of pulsars at higher spin down luminosity.

The spin period distribution in Fig. 20 shows some simulated pulsars with a low spin period, in excess compared to the observations. This artifact disappears when the Gaussian distribution in log space for the spin period is used. The log-normal distribution enables to remove those pulsars in excess and make the distribution of the spin period better fit the observations. The KS test was also conducted on both P and \dot{P} and we find p-values, once again, considerably below 0.05 for both quantity, therefore rejecting the null hypothesis. We conclude that the initial distribution for the spin period found by Igoshev et al. (2022) allows to better reproduce the canonical pulsars population.

3.5. Gamma-ray detection

Let us now focus on the γ -ray band of the pulsar population. First, we note that the total number of pulsars detected simultaneously in gamma-ray and in radio is significantly larger in our simulation compared to the observations, when using the Fermi/LAT instrument sensitivity. However, the simulated gamma-ray pulsars are in the expected area of Fig. 21, meaning the striped wind model allow to correctly reproduce these pulsars. The explanation of this higher number of detection would be that there are many unidentified sources in the Fourth Fermi-LAT Catalog of Gamma-ray sources (4FGL). Since many unidentified Galactic sources are listed in these catalogs, many gamma-ray pulsars might have been detected without being identified as such yet. Furthermore, we can compare our results with the PPS work of Pierbattista et al. (2012), where they simulated the young gamma-ray pulsars population with 4 different models : Outer Gap (OG), Slot Gap (SG), Polar Cap (PC) and Outer Polar Cap (OPC) models. In summary their best model was the OPC model, which shows almost identical results as ours

(the $P-\dot{P}$ shape and the number of detection), except the fact that we detect gamma-ray pulsars a little further away from Earth.

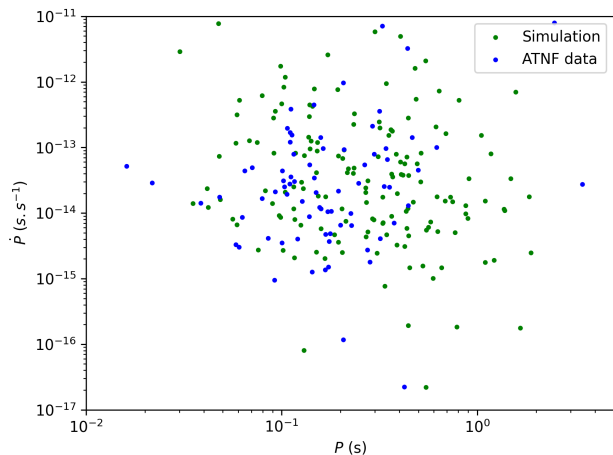


Fig. 21. $P - \dot{P}$ diagram of the gamma-only pulsars for both the simulations and the observations, with 1 million pulsars simulated.

What if we run another simulation (with the same parameters as in Table 5), by only changing the threshold of detection for gamma-ray? We did this in order to see how many more pulsars we would detect in gamma-ray and where they would be in the $P - \dot{P}$ diagram, and also to deal with the problematic of the GeV excess in the Galactic centre. Therefore we increased F_{\min} by 10: if the galactic latitudes of the pulsar is $< 2^\circ$, then $F_{\min} = 0.4 \times 10^{-15} \text{ W.m}^{-2}$, and concerning blind searches $F_{\min} = 1.6 \times 10^{-15} \text{ W.m}^{-2}$.

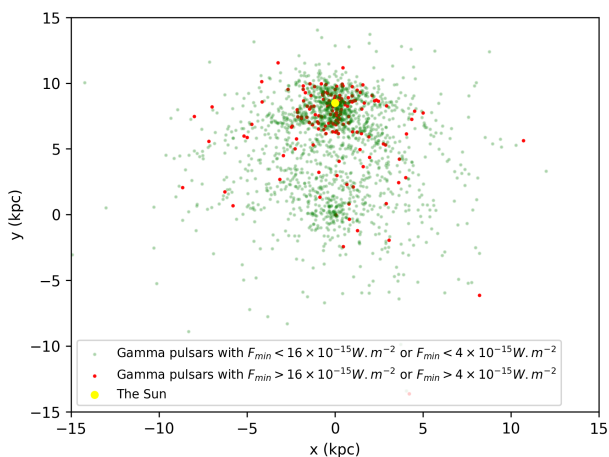


Fig. 22. Spatial distribution of the simulated gamma-ray detected pulsars, projected onto the Galactic plane for 1 million pulsars simulated, with a lower F_{\min} .

The gamma-ray detected pulsar positions in the X-Y plane of the Galaxy are shown in Fig. 22. In this simulation, 1832 gamma-ray pulsars are detected, among them only 168, in red in Fig. 22, would have been detected if the same sensitivity as before was kept. Therefore we detect 11 times more gamma-ray pulsars compared to the number found with the previous sensitivity. Furthermore, the other 1664 pulsars, in green in Fig. 22, detected with this increased sensitivity highlight sev-

eral features. We obviously detect more pulsars close to us, and also many more in the centre of the Galaxy. This result indicates that the GeV excess in the Galactic centre could be linked to pulsars not yet identified, while usually the hypothesis is that the GeV excess corresponds to self-annihilating dark matter particles (Hooper 2022). In addition, millisecond pulsars, not modeled in this work, could however also contribute to this GeV excess.

4. Discussion

For the initial spin period distribution Igoshev et al. (2022) suggested values for the mean period P_{mean} in the range from approximately 57 ms to 129 ms and for the spread σ_p the range from 0.45 to 0.65. The values $P_{\text{mean}} = 129 \text{ ms}$ and $\sigma_p = 0.45$ are best educated guesses. However it is obvious that further investigations could benefit from an automated method to find the best set of values. Hence, we are currently working on an optimization algorithm to find the optimal initial parameters for the population synthesis, not only for the spin period, but for the whole parameter space presented in Table 5, except for α_d and k_{τ_d} . Our optimization algorithm will help to constrain the properties of the Milky Way pulsar population by constraining parameters like the birth rate which is supposed to be between $1/33 \text{ yr}^{-1}$ and $1/150 \text{ yr}^{-1}$, see Faucher-Giguère & Kaspi (2006), Gullon et al. (2014) or Johnston & Karastergiou (2017).

We also added the effect of the ISM on the radio pulse profile, rendering more difficult to observe pulsars farther away than 10 kpc. Furthermore, because of this plasma propagation effect fewer radio pulsars are detected compared to the observations. If the simulations discard the ISM effect, much more pulsars are detected at distances larger than 10 kpc and with higher \dot{E} as well, improving the match between the simulation and the observation. Perhaps, the effect of the ISM is overestimated when computing the scattering and dispersion effect converted in equation (28a) with τ_{scat} and τ_{DM} is too important and should have less influence on the observed width pulse profile, therefore with formulas that would give lower τ_{DM} and τ_{scat} , we might get more realistic results.

In the main part of the paper, we abstain from showing outcomes stemming from simulations featuring a constant magnetic field. However we ran such simulations that clearly highlight the inferior performance of a simulation without magnetic field evolution as can be checked in appendix B. Moreover appendix C explores different parameter spaces for the PPS in order to meticulously scrutinizing whether the parameters showcased in the main part of the paper optimally encapsulate observational data. This demonstrates that even if a substantial number of parameters are required for the PPS, they can be meaningfully constrained by such studies with reasonable accuracy.

Furthermore, in Subsection 3.5 we explore the results when the sensitivity in gamma-ray is increased by a factor of 10. However we did not show what would happen if we tried to make a prediction for the radio detection by increasing the sensitivity by a factor of 50 to match approximately the properties of SKA. A simulation was run with this increased sensitivity and 52276 pulsars were detected (when simulating 1 million pulsars, with a death line), therefore approximately 31 times more than with the sensitivity of Parkes and Arecibo telescopes.

5. Summary

Without the implementation of the Galactic potential, in the PPS of Dirson et al. (2022), the pulsars were moving in straight lines

along one direction chosen randomly for each pulsar. This evolution of the proper motion was not realistic, even though the evolution model had already replicated a significant portion of the canonical pulsar population. However all the new improvements put into this PPS, meaning : the Galactic potential, the effect of the ISM on the radio pulse profiles and the fact that the decay timescale of the magnetic field is taken randomly within a certain range, allow a more accurate reproduction of the population in the $P - \dot{P}$ diagram.

The first results where we emulate 10 millions pulsars showed an excess of old pulsars detected in the simulation. In the $P - \dot{P}$ diagram we saw that this excess was associated to pulsars which lie below the death line, therefore, not creating pairs anymore. With this finding we realized that it was imperative to implement the death line. The results obtained with the death line were then in better agreement with observations when plotting the most relevant distributions such as period and period derivative.

Nonetheless, simulating 1 million pulsars allowed to show that with or without death line the results were alike and therefore, in the case where the oldest pulsar simulated is 4.1×10^7 yr, a death line is not really necessary to explain the observations. In this paper we showed two approach to reproduce the observed canonical pulsars population, however when we consider the approach where the oldest pulsar simulated is only 4.1×10^7 yr we state that no older pulsars might exist in the Galaxy, while the Milky Way is very much older than this. There is apparently no reason to not simulate pulsars that are older than this, and if there is one we do not know it (they become harder to detect because of their wide pulse profile with their age, but some are still detectable). If this situation is the reality then it means two things : the age of the observed pulsars are overestimated (because we observe pulsars older than 4.1×10^7 yr in the canonical population, even if they are not numerous) and the death line is not necessary in pulsar population synthesis work to explain what we observe. When the simulation is ran with 10 millions pulsars, the death line becomes a necessity. However this simulation gives results less similar to the observations, because of a few simulated data which do not match any observational data.

It was also shown that the old pulsars with age larger than 10 Myr have a tendency to lose their alignment between rotation axis and velocity, a direct effect of the Galactic potential as shown by the observations of Noutsos et al. (2013), but it is the first time it is done in a simulation.

The striped wind model seems to reproduce the gamma-ray population of canonical pulsars very well, however in the simulation a higher number of these pulsars are detected compared to reality. It probably indicates that a part of unidentified sources from the 4FGL catalog are pulsars. Testing an increased sensitivity for the detection of gamma-ray pulsars lead us to think that a part of the origin of the GeV excess in the Galactic centre could be young gamma-ray pulsars, and when the millisecond pulsars will be modeled in our simulation we would also be able to check that these pulsars might be responsible for this GeV excess. The usual picture is to suppose that only millisecond pulsars are responsible, while young gamma-ray pulsars could also play a role.

In summary, the best parameters found for this pulsar population synthesis are for $P_{\text{mean}} = 129$ ms, $\sigma_p = 0.45$ for the spin period distribution at birth, $B_{\text{mean}} = 2.75 \times 10^8$ T, $\sigma_b = 0.5$ for the magnetic field distribution at birth and for a birth rate of $1/41 \text{ yr}^{-1}$. Ultimately, this work provides a simulated population of pulsars within the Milky Way more similar to the observations compared to Johnston et al. (2020) and Dirson et al. (2022), the

two most recent population synthesis considering both radio and gamma-ray emission. Moreover, such investigations will be useful to make more predictions for future radio surveys such as SKA, or NenuFAR.

The PPS method used in this study could be applied to model populations of pulsars in the Milky Way other than the canonical ones. The magnetars, for instance, would need : another distribution at birth for their magnetic field to be modeled correctly, taking into account the emission in X-rays and having a faster decay for the magnetic field. The magnetars are the pulsars just above the canonical pulsars in the $P - \dot{P}$ diagram, at the top right of the diagram. A more complex population is the recycled or millisecond pulsars, that were "brought back to life" by accreting matter from a companion star. This accretion mechanism spins up the neutron stars moving them from the graveyard of pulsars to the bottom left of the $P - \dot{P}$ diagram, crossing again the death line in the opposite sense and allowing them to create electron-positron pair cascades again. However, they are more complex to model because this evolution scenario should take into account the accretion process and spin-up. We are also currently working on both populations to reproduce them in a PPS based on this work.

Acknowledgements. This work has been supported by the grant ANR-20-CE31-0010. We acknowledge the High Performance Computing Centre of the University of Strasbourg for supporting this work by providing scientific support and access to computing resources. D.M. acknowledges the support of the Department of Atomic Energy, Government of India, under project No. 12-R&DTFR-5.02-0700.

References

- Abdo, A. A., Ajello, M., Allafort, A., et al. 2013, ApJS, 208, 17
 Ahlers, Markus ; Bai, Yang ; Barger, Vernon ; Lu, Ran, Physical Review D, Volume 93, Issue 1, id.013009
 Arons, J. 1983, ApJ, 266, 215
 Bajkova, A. T., Bobylev, V. V. Astronomical & Astrophysical Transactions, 2021, Vol. 32, Issue 3, pp. 177-206
 Bates, S. D., Lorimer, D. R., Rane, A., & Swiggum, J. 2014, MNRAS, 439, 2893
 Bogdanov, S., Lamb, F. K., Mahmoodifar, S., et al. 2019, ApJ, 887, L26
 Bovy, J. The Astrophysical Journal Supplement Series, Volume 216, Issue 2, article id. 29, 27 pp. (2015)
 Cameron A. D., et al., 2020, MNRAS, 493, 1063
 Chen, Kaiyou ; Ruderman, Malvin, January 1993, Astrophysical Journal v.402, p.264
 Cheng, K. S., Ho, C., & Ruderman, M. 1986, ApJ, 300, 500
 Cordes, J. M., & McLaughlin, M. A. 2003, ApJ, 596, 1142
 Cordes J. M., et al., 2006, ApJ, 637, 446
 Daugherty, J. K., & Harding, A. K. 1982, ApJ, 252, 337
 Daugherty, J. K., & Harding, A. K. 1996, ApJ, 458, 278
 Dirson, P etri, and Mitra 2022, Astronomy & Astrophysics, Volume 667, id.A82, 12 pp.
 Faucher-Gigu ere, C.-A., Kaspi, V. M. 2006, ApJ, 643, 332
 Gil, Janusz ; Mitra, Dipanjan, The Astrophysical Journal, Volume 550, Issue 1, pp. 383-391, March 2001
 Gonthier, Peter L.; Harding, Alice K.; Ferrara, Elizabeth C. ; Frederick, Sara E.; Mohr, Victoria E. ; Koh, Yew-Meng, The Astrophysical Journal, Volume 863, Issue 2, article id. 199, 27 pp. (2018)
 Gonthier, Peter L. ; Ouellette, Michelle S. ; Berrier, Joel ; O'Brien, Shawn ; Harding, Alice K. The Astrophysical Journal, Volume 565, Issue 1, pp. 482-499, January 2002
 Graber, Vanessa ; Ronchi, Michele ; Pardo-Araujo, Celsa ; Rea, Nanda, eprint arXiv:2312.14848
 Gull on, M., Miralles, J. A., Vigan o, D., Pons, J. A. 2014, MNRAS, 443, 1891
 Harding, A. K., Stern, J. V., Dyks, J., Frackowiak, M. 2008, ApJ, 680, 1378
 Harding, A. K., Muslimov, A. G. 2011, ApJ, 743, 181
 Hewish, A. ; Bell, S. J. ; Pilkington, J. D. H. ; Scott, P. F. ; Collins, R. A. Nature, Volume 224, Issue 5218, pp. 472 (1969)
 Hobbs, G., Lorimer, D. R., Lyne, A. G., Kramer, M. 2005, MNRAS, 360, 974
 Hofmann & Zanin, May 2023, eprint arXiv:2305.12888
 Hooper, Dan, September 2022, eprint arXiv:2209.14370
 Hirotani, K. 2008, ApJ, 688, L25

- Igoshev, Andrei P., Frantsuzova, Anastasia, Gourgouliatos, Konstantinos, N. Monthly Notices of the Royal Astronomical Society, Volume 514, Issue 3, pp. 4606-4619
- Jawor, J.A., Tauris, T.M. Monthly Notices of the Royal Astronomical Society, Volume 509, Issue 1, pp.634-657, 2022
- Johnston, S., Karastergiou, A. Monthly Notices of the Royal Astronomical Society, Volume 467, Issue 3, p.3493-3499, 2017
- Johnston, Simon ; Karastergiou, A., Monthly Notices of the Royal Astronomical Society, Volume 485, Issue 1, p.640-647
- Johnston, S., Smith, D. A., Karastergiou, A., Kramer, M. 2020, MNRAS, 497, 1957
- Johnston et al., Monthly Notices of the Royal Astronomical Society, Volume 520, Issue 4, pp.4801-4814
- Kalapotharakos, C., Harding, A. K., Kazanas, D., Wadiasingh, Z. 2019, ApJ, 883, L4
- Kramer M., et al., 2003, MNRAS, 342, 1299
- Krishnakumar, M. A., Mitra, D., Naidu, A., Joshi, B. C., & Manoharan, P. K. 2015, ApJ, 804, 23
- Li, C., Zhao, G., Jia, Y., et al. 2019, ApJ, 871, 208
- Lorimer, D. R., Kramer, M. 2004, Handbook of Pulsar Astronomy
- Lorimer D. R., et al., 2006, ApJ, 640, 428
- Manchester, R. N., Hobbs, G. B., Teoh, A., Hobbs, M. 2005, AJ, 129, 1993
- McMullin et al., Proceedings of the SPIE, Volume 11445, id. 1144512 18 pp. (2020)
- Mitra, D. 2017, J. Astrophys. Astron., 38, 52
- Mitra, D., Basu, R., Melikidze, G. I., Arjunwadkar, M. Monthly Notices of the Royal Astronomical Society, Volume 492, Issue 2, p. 2468-2480
- Miyamoto & Nagai, Publications of the Astronomical Society of Japan, Vol. 27, 533-543 (1975)
- Muslimov, A. G., Harding, A. K. 2004, ApJ, 617, 471
- Navarro, Frenk, White, The Astrophysical Journal, Volume 490, Issue 2, pp. 493-508
- Noutsos, A., Schnitzeler, D. H. F. M., Keane, E. F., Kramer, M., Johnston, S. Monthly Notices of the Royal Astronomical Society, Volume 430, Issue 3, p. 2281-2301
- Paczynski, Bohdan, Astrophysical Journal v.348, p. 485
- Peter Young. The leapfrog method and other "symplectic" algorithms for integrating Newton's laws of motion. 2014.
- Pétri, J. 2009, A&A, 503, 13
- Pétri, J. 2011, MNRAS, 412, 1870
- Pétri, J. 2012, MNRAS, 424, 605
- Philippov, A., Tchekhovskoy, A., Li, J. G. 2014, MNRAS, 441, 1879
- Pierbattista, M. ; Grenier, I. A.; Harding, A. K. ; Gonthier, P. L., Astronomy & Astrophysics, Volume 545, id.A42, 23 pp., September 2012
- Popov, S. B. ; Pons, J. A. ; Miralles, J. A. ; Boldin, P. A. ; Posselt, B, MNRAS, Volume 401, Issue 4, pp. 2675-2686, February 2010
- Rankin, Joanna M, The Astrophysical Journal, Volume 664, Issue 1, pp. 443-447
- Riley, T. E., Watts, A. L., Bogdanov, S., et al. 2019, ApJ, 887, L21
- Ronchi, M. ; Graber, V.; Garcia-Garcia, A.; Rea, N.; Pons, J. A., The Astrophysical Journal, Volume 916, Issue 2, id.100, 20 pp.
- Ruderman, M. A., Sutherland, P. G. 1975, ApJ, 196, 51
- Siegert, T. 2019, A&A, 632, L1
- Skowron, D. M., Skowron, J., Mróz, P., et al. 2019, Sci, 365, 478
- Smirnov, N. (1948). Table for estimating the goodness of fit of empirical distributions. Annals of Mathematical Statistics, 19(2), 279-281.
- Smith, D. A., Bruel, P., Cognard, I., et al. 2019, ApJ, 871, 78
- Smith et al., The Astrophysical Journal, Volume 958, Issue 2, id.191, 72 pp.
- Spitkovsky, Anatoly, The Astrophysical Journal, Volume 648, Issue 1, pp. L51-L54
- Sturrock, P. A. 1971, ApJ, 164, 529
- Takata, J., Wang, Y., Cheng, K. S. 2011, ApJ, 726, 44
- van der Kruit, P. C. in Comparison of the Galaxy with External Spiral Galaxies, eds. G. Gilmore, & B. Carswell (Dordrecht: Springer, Netherlands), 27
- Viganò, D. 2013, ArXiv e-prints [arXiv:1310.1243]
- Viganò, D., Rea, N., Pons, J. A., et al. 2013, MNRAS, 434, 123
- Watters, K. P., Romani, R. W. 2011, ApJ, 727, 123
- Weltevrede, Patrick ; Johnston, Simon, Monthly Notices of the Royal Astronomical Society, Volume 391, Issue 3, pp. 1210-1226
- Yadigaroglu, I.-A., Romani, R. W. 1995, ApJ, 449, 211
- Yao, J. M. ; Manchester, R. N. ; Wang, N., The Astrophysical Journal, Volume 835, Issue 1, article id. 29, 32 pp. (2017).
- Zhang, Bing ; Harding, Alice K. ; Muslimov, Alexander G., The Astrophysical Journal, Volume 531, Issue 2, pp. L135-L138, March 2000

Appendix A: The integration scheme used

A.1. The scheme

One of the new aspect in this work is to solve the equation of motion (12) in order to follow more realistically the motion of our sample of pulsars. To achieve this objective we implemented a fourth order integration scheme called Position Extended Forest Ruth-Like (PEFRL). This algorithm was chosen because of its high order allowing a high precision on the trajectory of the pulsar. In addition, it is a symplectic algorithm, meaning that it conserves the total energy of the pulsar (kinetic plus potential), minimizing the error even if the integration is done for a long time with any orbits. It works in the same way as a Verlet scheme of second order, the velocities and coordinates are shifted separately but in the end they get synchronized. The different steps of the algorithm are as follows

$$\mathbf{r}^{n+\frac{1}{5}} = \mathbf{r}^n + \xi h \mathbf{v}^n \quad (\text{A.1a})$$

$$\mathbf{v}^{n+\frac{1}{4}} = \mathbf{v}^n - (1 - 2\lambda) \frac{h}{2} \nabla \Phi(\mathbf{r}^{n+\frac{1}{5}}) \quad (\text{A.1b})$$

$$\mathbf{r}^{n+\frac{2}{5}} = \mathbf{r}^{n+\frac{1}{5}} + \chi h \mathbf{v}^{n+\frac{1}{4}} \quad (\text{A.1c})$$

$$\mathbf{v}^{n+\frac{3}{4}} = \mathbf{v}^{n+\frac{1}{4}} - \lambda h \nabla \Phi(\mathbf{r}^{n+\frac{2}{5}}) \quad (\text{A.1d})$$

$$\mathbf{r}^{n+\frac{3}{5}} = \mathbf{r}^{n+\frac{2}{5}} + (1 - 2(\chi + \xi)) h \mathbf{v}^{n+\frac{3}{4}} \quad (\text{A.1e})$$

$$\mathbf{v}^{n+\frac{3}{4}} = \mathbf{v}^{n+\frac{3}{4}} - \lambda h \nabla \Phi(\mathbf{r}^{n+\frac{3}{5}}) \quad (\text{A.1f})$$

$$\mathbf{r}^{n+\frac{4}{5}} = \mathbf{r}^{n+\frac{3}{5}} + \chi h \mathbf{v}^{n+\frac{3}{4}} \quad (\text{A.1g})$$

$$\mathbf{v}^{n+1} = \mathbf{v}^{n+\frac{3}{4}} - (1 - 2\lambda) \frac{h}{2} \nabla \Phi(\mathbf{r}^{n+\frac{4}{5}}) \quad (\text{A.1h})$$

$$\mathbf{r}^{n+1} = \mathbf{r}^{n+\frac{4}{5}} + \xi h \mathbf{v}^{n+1} \quad (\text{A.1i})$$

here \mathbf{r} is the position vector, \mathbf{v} is the velocity vector, h is the time step, $\nabla \Phi$ is the gradient of the potential and n is the time at which we compute the position or the velocity. λ , ξ and χ are constants that are tabulated in Table A.1, see for instance Peter Young (2014).

Table A.1. Value of the constants used for the PEFRL scheme.

| Parameters | Values |
|------------|----------------------|
| λ | -0.212341831062605 |
| ξ | 0.178617895844809 |
| χ | -0.06626458266981849 |

A.2. Precision of the PEFRL algorithm

Before implementing the gravitational potential and the integration scheme in the whole synthesis, the precision of the trajectory of a single pulsar in the Milky Way was checked. The initial conditions for the pulsar are the following : $x = 5.1$ kpc, $y = -1.9$ kpc, $z = 0.05$ kpc, $v_x = -47.8$ km/s, $v_y = 97.0$ km/s, and $v_z = 22.6$ km/s. Those initial conditions were chosen randomly, the only constrain being to have the pulsar in the Galaxy with realistic coordinates on the one hand and with realistic speeds for a pulsar on the other hand. Furthermore, the total integration time is 1.25 Gyr and the time step used is 10^5 yr. In order to check the precision of the scheme, the total energy of the pulsar, sum of the kinetic plus potential energy, that should be conserved is computed as

$$E_{tot} = \frac{v_x^2}{2} + \frac{v_y^2}{2} + \frac{v_z^2}{2} + \Phi_{tot}. \quad (\text{A.2})$$

The trajectory obtained after the integration with the PEFRL algorithm is shown in Fig. A.1. This trajectory shows that the pulsar, with these initial conditions, remains bound to the Galaxy. The pulsar here takes approximately 201.3 Myr to complete an orbit in the Galaxy. The time step chosen is significantly smaller than the orbital period ($h/P_{orb} = 0.0005$), and we obtain approximately 6 orbits by integrating the trajectory during 1.25 Gyr. Bajkova & Bobylev (2021) showed several trajectories in their paper, the one obtained here seems coherent compared to the different trajectories that they got.

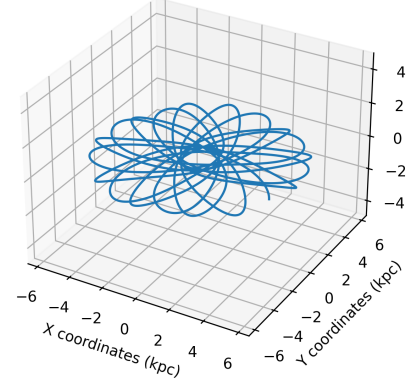


Fig. A.1. Trajectory of a single pulsar in the Galactocentric frame.

Fig. A.2 shows the relative error on the total energy. It is indeed almost constant along the whole integration of the trajectory. The maximum relative error on the energy is of the order of 10^{-9} , a very good accuracy for this trajectory. Globally, when a single pulsar has its trajectory integrated in the PPS, the relative error is at maximum 0.001 and the minimum seen was 10^{-14} .

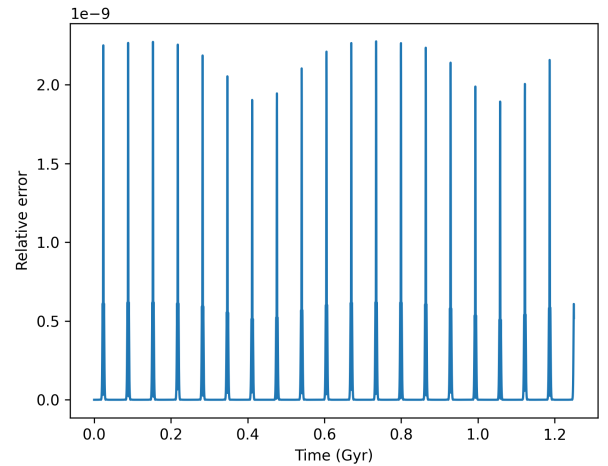


Fig. A.2. Relative error on the energy of a single pulsar in the Galactocentric frame.

Appendix B: Results for a constant magnetic field

Depending on the PPS, the magnetic field will be considered constant (Johnston & Karastergiou 2017; Faucher-Giguère &

Kaspi 2006) or decaying (Gullon et al. 2014; Dirson et al. 2022; Jawor & Tauris 2022). The goal is here is to show the results with a constant magnetic field in order to see which model is better between the decaying magnetic field and the constant magnetic field.

Hence, this simulation was run with 1 million pulsar simulated, without a death line and without a decaying of the magnetic field. The KS test gave p-values of 6.3×10^{-22} and 9.8×10^{-77} , therefore the null hypothesis is rejected for both P and \dot{P} . The parameters used are in Table 5. It is less good than with a decaying magnetic field. As can be seen in Fig. B.1, too many pulsars from the simulation appear on the top right of the diagram and almost none at the bottom. In Table B.1, we note a total of pulsars which is smaller from what we found for all of our previous results in Sect. 3.

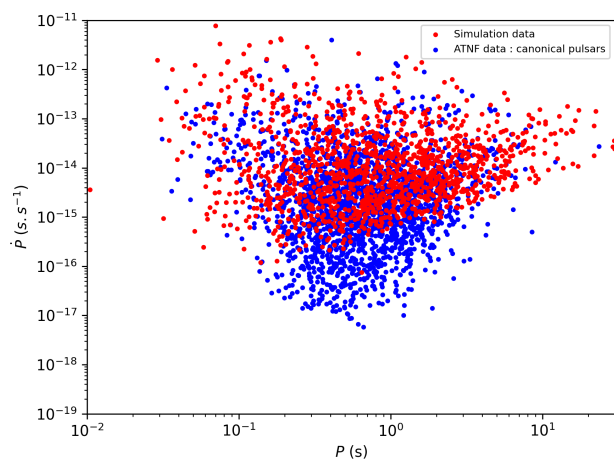


Fig. B.1. $P - \dot{P}$ diagram of the simulated population, along with the observations, with the death line implementation and a constant magnetic field for each pulsar.

Table B.1. Number of pulsars detected for the simulation with constant magnetic field for each pulsar and the death line implementation.

| $\log(\dot{E})$ (W) | N_{tot} | N_r | N_g | N_{rg} |
|---------------------|-----------|-------|-------|----------|
| >31 | 15 | 0 | 12 | 3 |
| >28 | 168 | 4 | 94 | 70 |
| Total | 1356 | 1034 | 162 | 160 |

Appendix C: Influence of the different parameters

In order to show that the parameters chosen in the main part of this paper are meticulously picked and that the uncertainties brought by the large number of parameters is manageable, several simulations were run with different values for the main parameters of the initial distributions, showing a deviation from the best values gives bad results. The simulations were run with in the same conditions as Subsection 3.2, with only one parameter changing between the different sets of simulation.

The $P - \dot{P}$ diagram of each simulation is not shown here because almost every simulation finds a too high (or too low) number of pulsars, therefore the $P - \dot{P}$ diagrams are showing large differences between observations and simulations. Nonetheless, the number of pulsars detected for two of the simulations with different P_{mean} (with $P_{mean} = 70$ ms and $P_{mean} = 100$ ms) gives

Table C.1. Influence of the birth rate.

| Birth rate (in yr^{-1}) | N_{tot} | N_r | N_g | N_{rg} |
|-----------------------------------|-----------|-------|-------|----------|
| 1/30 | 2388 | 1964 | 204 | 220 |
| 1/80 | 963 | 799 | 79 | 85 |
| 1/120 | 696 | 597 | 50 | 49 |

Table C.2. Influence of the mean initial period.

| P_{mean} (in ms) | N_{tot} | N_r | N_g | N_{rg} |
|--------------------|-----------|-------|-------|----------|
| 57 | 1499 | 1134 | 193 | 172 |
| 70 | 1623 | 1253 | 215 | 155 |
| 100 | 1652 | 1348 | 151 | 153 |

Table C.3. Influence of the mean initial magnetic field.

| B_{mean} (in T) | N_{tot} | N_r | N_g | N_{rg} |
|-------------------|-----------|-------|-------|----------|
| 10^7 | 8407 | 6943 | 406 | 1058 |
| 5×10^7 | 4447 | 3646 | 306 | 495 |
| 5×10^8 | 1111 | 933 | 109 | 69 |

number closer to reality. However their p-values for P and \dot{P} when using the KS test were significantly below 0.05, which allowed us to reject the null hypothesis for the distributions of P and \dot{P} , for the results shown in Table C.1, C.2 and C.3.

Moreover in order to get an idea on a good range of values for the parameters, the d-value obtained thanks to the KS test are shown in Table C.4, C.5, C.6 and C.7. For each parameter, 10 simulations were made in order to get a mean and a standard deviation for the d-value associated. These simulations helped finding the best values for the parameters by considering the parameter is well constrained when its d-values for both distribution of P and \dot{P} are below, or really close to 0.05 (meaning 5 % similarity between the observations and simulation distribution). Even though it is not an optimisation (and therefore the results can be improved on that point), it allows us to conclude that P_{mean} should be between 120 ms and 135 ms (with 129 ms as best value). B_{mean} should be between 2.25×10^8 T and 2.8×10^8 T (with 2.75×10^8 T as best value). The birth rate should be between $1/37 \text{ yr}^{-1}$ and $1/45 \text{ yr}^{-1}$ (with $1/41 \text{ yr}^{-1}$ as best value). Finally, σ_b is well constrained between 0.49 and 0.51 (with 0.5 as best value). Concerning σ_p , it always gives d-values between 0.04 and 0.057 when σ_p is below 0.6, therefore the value 0.45 was chosen as suggested by Igoshev et al. (2022).

Table C.4. D-value for different P_{mean} .

| P_{mean} (in ms) | d-value (\dot{P}) | d-value (P) |
|--------------------|-----------------------|----------------------|
| 90 | 0.072 ± 0.0073 | 0.0577 ± 0.0080 |
| 100 | 0.0651 ± 0.00692 | 0.0503 ± 0.00636 |
| 110 | 0.0652 ± 0.00688 | 0.0381 ± 0.0074 |
| 120 | 0.0554 ± 0.00714 | 0.0302 ± 0.00468 |
| 129 | 0.0557 ± 0.00740 | 0.0284 ± 0.00583 |
| 135 | 0.0544 ± 0.00768 | 0.0329 ± 0.00767 |
| 150 | 0.0572 ± 0.00779 | 0.0388 ± 0.00935 |

Table C.5. D-value for different B_{mean} .

| B_{mean} (in T) | d-value (\dot{P}) | d-value (P) |
|--------------------------|-----------------------|----------------------|
| 1×10^8 | 0.113 ± 0.00823 | 0.203 ± 0.00675 |
| 2×10^8 | 0.0418 ± 0.00459 | 0.0658 ± 0.00705 |
| 2.25×10^8 | 0.0456 ± 0.00455 | 0.0455 ± 0.0061 |
| 2.75×10^8 | 0.0557 ± 0.00740 | 0.0284 ± 0.00583 |
| 2.8×10^8 | 0.0576 ± 0.00907 | 0.0298 ± 0.00728 |
| 3×10^8 | 0.0648 ± 0.01092 | 0.0426 ± 0.00775 |
| 3.25×10^8 | 0.0761 ± 0.00930 | 0.0480 ± 0.00997 |

Table C.6. D-value for different σ_b .

| σ_b | d-value (\dot{P}) | d-value (P) |
|------------|-----------------------|----------------------|
| 0.45 | 0.0767 ± 0.00668 | 0.0513 ± 0.01258 |
| 0.48 | 0.0621 ± 0.00880 | 0.0385 ± 0.01234 |
| 0.49 | 0.0646 ± 0.00974 | 0.0304 ± 0.00501 |
| 0.5 | 0.0557 ± 0.00740 | 0.0284 ± 0.00583 |
| 0.51 | 0.056 ± 0.00735 | 0.0306 ± 0.00701 |
| 0.52 | 0.0547 ± 0.00786 | 0.0358 ± 0.00579 |

Table C.7. D-value for different birth rate (BR).

| BR (in yr^{-1}) | d-value (\dot{P}) | d-value (P) |
|---------------------------|-----------------------|----------------------|
| 1/33 | 0.0611 ± 0.01025 | 0.0313 ± 0.00636 |
| 1/37 | 0.0565 ± 0.00851 | 0.0295 ± 0.00645 |
| 1/41 | 0.0557 ± 0.00740 | 0.0284 ± 0.00583 |
| 1/45 | 0.0585 ± 0.00510 | 0.0302 ± 0.00565 |
| 1/70 | 0.0691 ± 0.00830 | 0.0342 ± 0.01165 |
| 1/150 | 0.1165 ± 0.01564 | 0.0408 ± 0.00671 |